Soft electronic vias and interconnects through rapid three-dimensional assembly of liquid metal microdroplets

Dong Hae Ho,[1,2,3] Chenhao Hu,[4,5] Ling Li,[4,5] and Michael D. Bartlett[1,2*]

[1]Mechanical Engineering, Soft Materials and Structures Lab, Virginia Tech, Blacksburg, VA 24061, USA.
[2]Macromolecules Innovation Institute, Virginia Tech, Blacksburg, VA 24061, USA.
[3]Present address: Department of Energy Science and Engineering, Daegu Gyeongbuk Institute of Science and Technology (DGIST), Daegu, 42988, Republic of Korea
[4]Mechanical Engineering, Virginia Tech, Blacksburg, VA 24061, USA.
[5]Present address: Department of Materials Science and Engineering, University of Pennsylvania, PA 19104, USA.

*To whom correspondence should be addressed: mbartlett@vt.edu

Cite this article: Ho, D. H., Hu, C., Li, L., and Bartlett, M. D., "Soft electronic vias and interconnects through rapid three-dimensional assembly of liquid metal microdroplets." *Nature Electronics* **7**, 1015-1024 (2024). https://www.nature.com/articles/s41928-024-01268-z

Abstract

The development of soft electronics requires methods to connect flexible and stretchable circuits. With conventional rigid electronics, *vias* are typically used to electrically connect circuits with multilayered architectures, increasing device integration and functionality. However, creating *vias* using soft conductors leads to additional challenges. Here, we show that soft *vias* and planar interconnects can be created through the directed stratification of liquid metal droplets with programmed photocuring. Abnormalities that occur at the edges of a mask during UV exposure are leveraged to create vertical stair-like architectures of liquid metal droplets within the photoresin. The liquid metal droplets in the uncured (liquid) resin rapidly settle, assemble, and then are fully cured, forming electrically conductive soft *vias* at multiple locations throughout the circuit in a parallel and spatially tunable manner. Our three-dimensional selective stratification method forms seamless connections with planar interconnects, for in-plane and thru-plane electrical integration.

To create highly integrated circuits,[1] multiple circuit layers can be connected with *vias* that electrically interconnect different layers.[2] For traditional, rigid electronics the fabrication of *vias* is well established. Silicon wafer level *vias* in micro-to-nanometre regions are created through chemical or plasma etching, and larger scale printed circuit board (PCB) *vias* are made with micro or laser drilling followed by electroplating or filling with conductive materials.[3]

For soft electronics — which are of use in soft robotics,[4–6] wearable electronics,[7–10] and flexible displays[11–13] — integration approaches and multilevel architectures are undeveloped compared with their rigid counterparts. The primary role of *vias* is to electrically connect different layers, but soft devices introduce several new challenges due to their mechanically dynamic and conformal nature. First, due to the mechanics of flexible substrates, *vias* can act as stress concentration points that induce structural flaws.[14] Second, rigid metallic *vias* in stretchable substrates can cause mechanical failure due to the modulus mismatch between the substrate and the *vias*.[15,16] Third, current fabrication techniques for creating *vias* typically involve a time-consuming multistep procedure such as epoxy resin/copper composite filling or electroless plating.[17–19] In addition, *via* fabrication in flexible electronics still relies on two-dimensional manual drilling procedures that are performed for every individual *via*. Therefore, while soft electronics have advanced tremendously in-plane, thru-plane integration presents challenges.

One approach to address these challenges is to use stretchable and flexible conductive materials, such as liquid metal (LM). LM has a combination of fluidity and high thermal and electrical conductivity,[20–24] allowing it to be used as an electrically conductive material in various flexible and stretchable electronics.[25–27] In addition, LM-based composites can incorporate high electrical/thermal conductivity into soft polymers.[28–32] LM has been used as a *via* material using various methods, including wetting or filling of the *via* holes,[33–37] lift-off patterning,[38] and using iron wires to make the through-hole and wetting it with LM.[39] However, these methods include multistep *via* fabrication techniques that make individual

holes using templates or drilling procedures, which are limited to the two-dimensional domain. LM filling techniques can also have interface problems. For example, the surface of the LM interconnect can be easily disturbed by physical deformation. Integrating LM with conventional solid electronic components can also cause bonding issues between the substrate and the solid electronics due to the fluidic nature of LM.

In this Article, we report a liquid metal programmed stratification technique to form soft vertical *vias* and interconnects between circuit layers. The process uses UV-curable photoresin containing dispersed LM microdroplets (LMMDs) as the circuit material. Placement of the liquid metal throughout the circuit volume is controlled by using a shadow mask to vary the exposure to UV light. Photoresin exposed to UV solidifies and LMMDs are fixed in place, while in areas not exposed the photoresist remains a liquid and LMMDs, which have a higher density, sink to the bottom. Our approach relies on an imperfect curing anomaly that occurs at the edges of the shadow mask, where the photoresin receives a smaller UV expose dose than centre regions and is only partially cured, to create a stair-like structure. The stair-like structure in the photoresin acts as a foundation for programmed settling and assembly of LM droplets, creating a continuous trace of LMMDs from the top to the bottom layer (Fig. 1a and Supplementary Video 1). This phenomenon occurs in under a minute and can create hundreds of *vias* across the plane simultaneously. This Liquid Metal Stratification for Three-dimensional Assembly of electrical InteRconnects (LM-STAIR) approach is a rapid and scalable approach to enable three-dimensional interconnected circuit designs in soft and flexible electronics.

In contrast to conventional *via* approaches, such as through hole and wire bonding, liquid metal stratification creates multilayer circuits without through holes or bond lines, forming robust connections in continuous films (Fig. 1b). Our approach offers desirable mechanical and electrical properties for soft and flexible devices, including tunable modulus and strain invariant electrical conductivity. We show that approach can be used to connect several circuits, including a hybrid electronic device that incorporates magnetic field sensing and

display functions on a single, double-sided device.

Results and Discussion

3D assembly of LM-STAIR soft *vias*

The curing behavior of photoresin enables LM-STAIR to create a continuous electrical path from the top to the bottom layer. The LM-STAIR approach is governed by two phenomena. First, selective curing of the photoresin. When the photoresin/diluent and LMMDs composite is exposed to UV, photoresin solidifies and the position of LMMDs is fixed within the cured region. However, areas not exposed to UV remain in the liquid state, allowing LMMDs to move freely inside the liquid-state photoresin. LMMDs have a higher density ($6.25\,\mathrm{g/cm^3}$) compared to the photoresin ($1.05\,\mathrm{g/cm^3}$), so that LMMDs in the uncured region can sediment due to gravity. Second, undercut behavior occurs at the edge of the shadow mask. When photoresin is exposed to UV, the curing reaction is focused in the center of the exposed area rather than the edges, which results in a convex curing profile (Figure S1).[40] The slope of the convex profile provides a 3D foundation for the LMMDs to settle and creates a continuous droplet film from the top to the bottom plane (Figure 1c right). The LMMDs are then electrically activated through the application of mechanical pressure to percolate the droplets and form a continuous conductive network. Other activation techniques, such as the use of acoustic fields,[30,32] can also be used to activate the LM networks, as shown in Figure S2 and Supplementary Video 2. By combining these two phenomena, we realized an intricate flexible double layer circuit where two different planes are electrically connected without a through-hole (Figure 1d). The presented sample circuit has parallel top and bottom planar interconnects that cross each other without causing a short circuit, resulting in illumination of both LEDs on the top and bottom sides of the plane. This parallel, two-level LM-STAIR fabrication method will be discussed further in a later section.

Directed stratification of LMMDs is presented in real time in Figure 1c left and Supple-

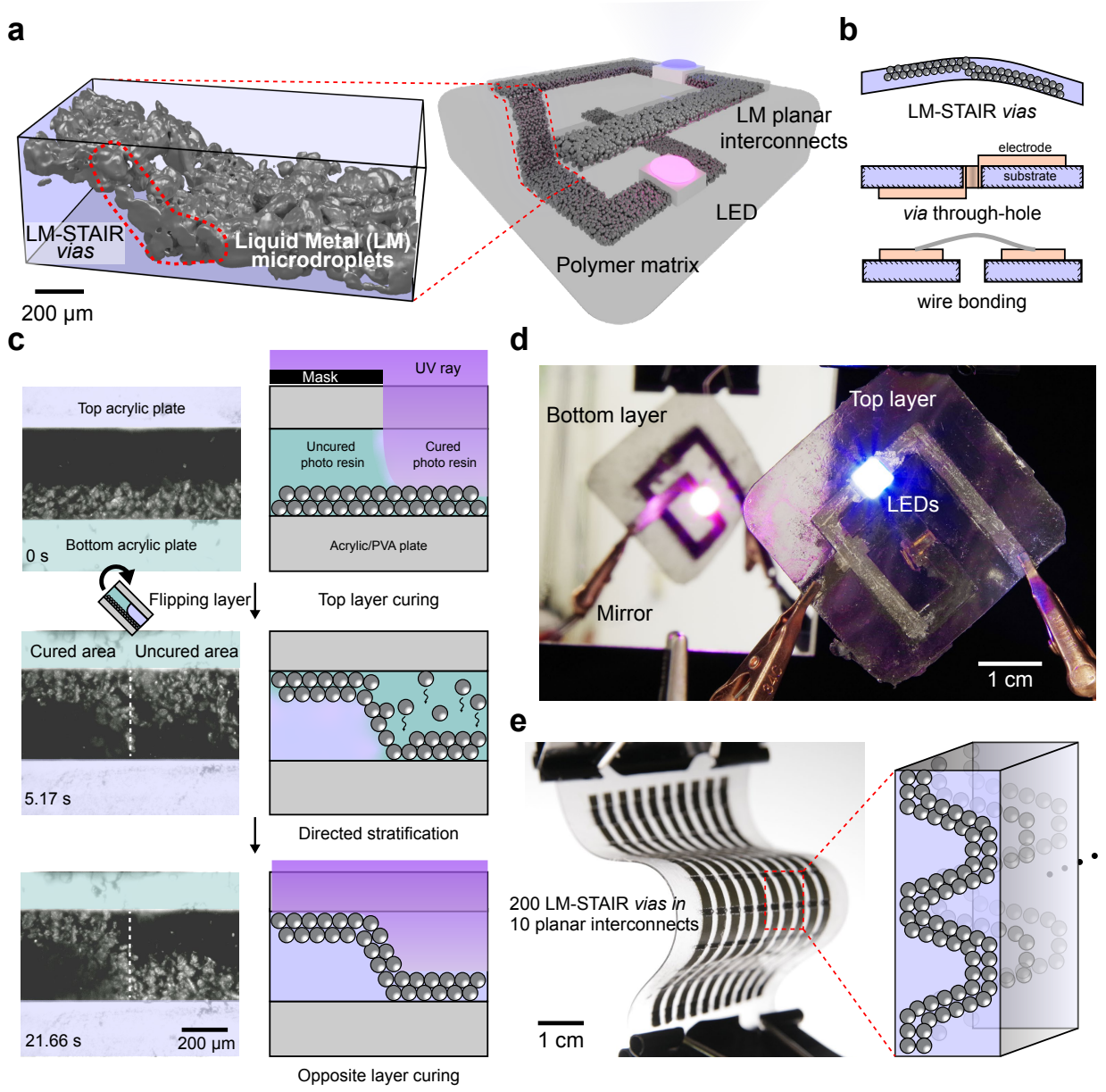

Fig. 1 | LM-STAIR fabrication of liquid metal soft interconnects and *vias*. **a**, Reconstructed microCT scan of LM-STAIR *vias* (left) and a schematic of a circuit that includes LM-STAIR *vias* seamlessly connecting top and bottom planar interconnects. **b**, Diagrams of representative electrical connection methods between two different planes. **c**, Images (left) and schematics (right) showing the directed stratification process of LMMDs. **d**, A functional circuit that includes a via junction and crossing top and bottom layer planar interconnects created through the LM-STAIR process. **e**, Photograph of a sample with 200 LM-STAIR *vias* in 10 planar electrodes and a diagram of LMMDs in the polymer matrix.

mentary Video 3. As shown in the photograph at 5.17 s, LMMDs inside the cured area are fixed in position. However, the LMMDs inside the uncured photoresin stratify to the bottom

giving rise to directed stratification and 3D control of LMMD connectivity. In contrast, previous LM composites that utilize sedimentation required long times (due to viscosity) and only focused on homogeneous settlement (i.e. the droplets settled throughout the entire composite),[28,29] while LM-STAIR utilizes heterogeneous and selective stratification that results in controlled 3D droplet architectures. One of the enabling aspects of LM-STAIR is that the LMMD stratification is completed in less than a minute and is not affected by the number and size of the *vias*. Therefore, the complexity of the circuit does not affect the processing time, unlike thru hole processes which create *vias* individually. Thus, LM-STAIR can be scaleable with a short processing time and large areal coverage. To demonstrate this, 10 linear stencil-printed LMMD planar interconnects are transformed into 200, 3D structured LM-STAIR *vias* through LM-STAIR in less than a minute (Figure 1e and Figure S3).

Mechanical characterization of LM-STAIR

The photoresin is composed of acrylate and methacrylate-based polymer, and dibutyltin dilaurate (Figure 2a). Adding a diluent, aliphatic monofunctional acrylate, softens the cured photoresin.[41] The weight percentage (wt%) of the diluent with the photoresin is modified to control the mechanical properties and the ratio will be donated as 30:70, e.g., 30 $wt\%$ of the photoresin and 70 $wt\%$ of the diluent. The volume fraction of LMMDs will be quantified by ϕ, where ϕ=volume of LMMDs / volume of (LMMDs + photoresin + diluent).

LMMDs are created using a shear mixing process (Figure 2b, left schematic), where a single large drop of LM in uncured photoresin breaks into LMMDs. The effect of shear mixing speed on the size of the LMMDs is measured by performing an image analysis on optical micrographs (Figure S4). The results indicate that the LMMD diameter plateaus at approximately 100 µm for the mixing condition of 2000 RPM after 2 minutes of mixing. Using a different combination of dilluent and viscosity modifier, smaller LMMD sizes can be achieved to decrease the minimum electrode width of the circuit electrodes (Figure 2c). We choose a shear mixing setup (2000 RPM, 2 minutes) that can produce the smallest LMMDs

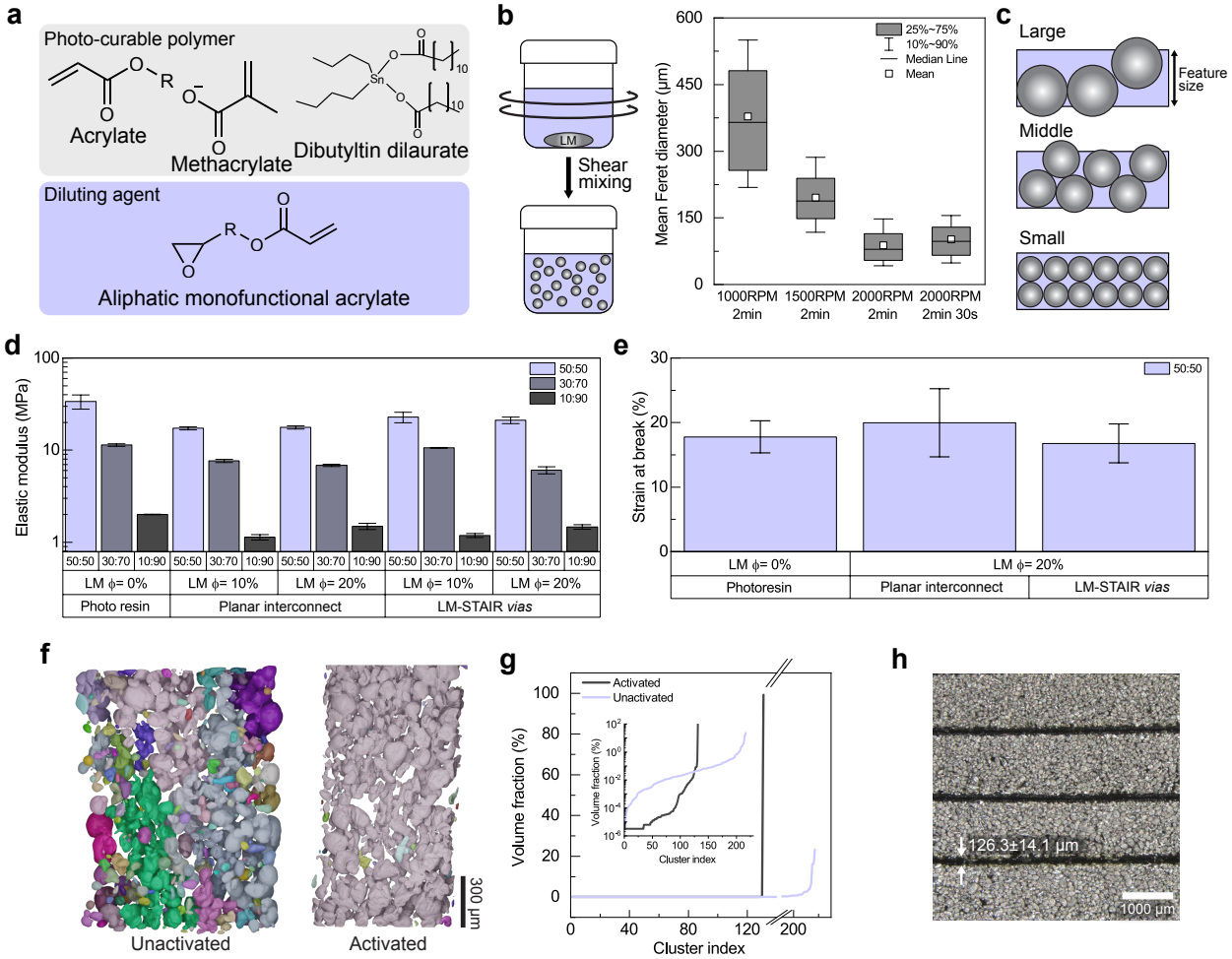

Fig. 2 | Physical characterization of LM-STAIR *vias* and interconnects. **a**, Chemical structure of the photocurable polymer and diluting agent. **b**, Analysis of LMMDs size based on shear mixing RPM and processing time. Data are collected from individual LMMD Feret diameters with the number of droplets for each bar is 41, 133, 448, and 493 (from left to right order). Data are presented as mean values ± standard deviation (s.d.). **c**, Diagram of circuit feature size based on LMMDs diameter. **d**, Young's modulus based on different ratios of photoresin, diluent, and LM volume percentage. The ratio presented as legend represents the weight ratio of photoresin and diluent (e.g., 30:70 denotes 30 $wt\%$ of photoresin and 70 $wt\%$ of diluent). LM is added to the uncured photoresin and diluent as the total volume percentage of the composite. **e**, Strain at break based on different ratios of photoresin, diluent, and LM volume percentage. Data in **d** and **e** are presented as the mean ± s.d. ($n = 3$ measurements from distinct samples). **f**, Reconstructed microCT images of unactivated and activated samples and the **g**, volume fraction analysis for each cluster. **h**, Optical microscopic image of the minimal gap between electrically conductive planar interconnects.

for the rest of the experiments.

To determine the appropriate polymer matrix for the LM-STAIR *via*, elastic modulus of

the photoresin/diluent without LMMDs is first measured (Figures 2d, S5 and S6). Elastic modulus of the cured pristine photoresin (100:0, ϕ= 0%) is measured as 1100 MPa which is higher than most soft and stretchable electronics (50 kPa $\sim$ 3 MPa).[42,43] Through the addition of diluent, the modulus of the polymer matrix decreases to 35 MPa (50:50, ϕ= 0%) and further to 2 MPa (10:90, ϕ= 0%). To make flexible and stretchable electric circuits, formulations containing $\leq$ 50 *wt*% photoresin are chosen to test elastic modulus of the composite that includes LMMDs.

To understand the effect of LMMDs in the polymer matrix, elastic modulus is measured for the planar line shape interconnect (planar interconnect) and the LM-STAIR *via* (Figure 2d). The results indicate that the inclusion of LMMDs causes a slight decrease in elastic modulus, which is consistent with the typical response when liquid fillers are added to a polymer or elastomer matrix.[44,45] In addition, the type of interconnect does not show any significant difference in elastic modulus. The strain at break for the selected samples is obtained from the same test. For a planar interconnect, the strain at break of ϕ= 10% and 20% LM shows 23.6 $\pm$ 0.8% and 20.0 $\pm$ 5.3%, respectively (Figure 2e and S7). These values are higher than ϕ= 0% LM sample of 17.7 $\pm$ 2.5%, showing that LMMDs do not degrade and potentially can improve the mechanical properties. LM-STAIR *vias* show similar strain at break of 16.8 $\pm$ 3.0% at ϕ= 20% LM compared to the non-LM photoresin (17.7 $\pm$ 2.5%).

MicroCT scans of the planar interconnect are taken to characterize the effective volume fraction of LM in the composite (Figure S8a). The LM volume fraction inside the composite is calculated from the reconstructed microCT image (Figure S8b). The planar interconnect has ϕ= 16.4% LMMDs inside the path, while the LM-STAIR *via* has ϕ= 14.5% LMMDs. Although the effective volume fraction of LMMDs is smaller than that of other LM-based composites ($\phi \geq$ 50%),[29,46,47] because of the confined concentration, it is possible to create a percolated conductive network at lower loadings of LMMDs.

To confirm this, the percolation network formation is observed by microCT (Figure 2f, Supplementary Video 4). The LMMDs are percolated using a mechanical embossing method

(i.e., activation process) that applies pressure to rupture the LMMDs and connect them (Figure S9). In Figure 2f, each color denotes a cluster that can be defined as a single connected droplet network. We find that the unactivated sample is a collection of individual or small clusters of droplets, however the nearly single-colored image of the activated sample shows that most of the LMMDs are connected as a single percolated conductive network. To quantify the connectivity of the unactivated and activated composite, the individual volume fraction of every cluster is graphed out (Figure 2g). The result shows that the largest cluster of unactivated droplets occupies 20% of the total 3D reconstructed volume, representing a discrete network. However, the largest cluster for the activated droplets occupies 99.3% of the total volume, which is indicative of a single continuous network.

We further examine the microCT data through percolation network analysis. The activated and unactivated samples are segmented into individual particles using the random-walk distance transforms (Figure S10).[48] The unactivated sample shape factor ($shape\ factor = \frac{Surface\ area^3}{36\times\pi\times Volume^2}$, perfect sphere = 1) shows a smaller distribution and lower average values compared to the activated samples, indicating that the activation process breaks the spherical shape of the LMMDs and transforms to a more irregular shape (Figure S10a). Additionally, the coordination number that refers to the number of connections between different LMMD increases as a result of activation (Figure S10b). Furthermore, Figure S10c shows that larger LMMDs tend to locate at the bottom of the composite and have a higher coordinate number, which agrees with the Stoke's law that larger LMMDs have higher settling velocity.[49] Also, larger LMMDs tend to form more connections due to their higher number of neighboring LMMDs. Taken together, these results support the formation of a controlled, 3D network of connected LMMDs in the LM-STAIR fabrication approach, and presents quantitative morphological evidence for LM network formation in general.

In addition, the minimum feature size of the stencil mask patterning method is investigated. As shown in Figure 2h and S11, the minimum gap between planar interconnects, and the minimum width of planar interconnect are 126 µm and 208 µm, respectively. The electri-

cal resistance of the minimum feature size planar interconnect (5 cm length) is measured to ensure that the LMMDs are electrically connected to each other (Figure S12). Electrical isolation between each planar interconnect is measured to ensure that traces are conductive but isolated from each other (Figure S13). The resolution of the stencil mask patterning method can be further improved using a more advanced stencil fabrication method and smaller LM droplets in the future. We further examined the applicability of LM-STAIR in four different acrylic and silicone-based photoresins. As shown in Figure S14, *vias* are successfully fabricated in all the resins, presenting the generalizable nature of LM-STAIR.

Electromechanical characterization of LM-STAIR

Along with the physical characteristics, the electromechanical properties of the fabricated samples are determined. During the electromechanical test, 50:50 photoresin/diluent polymer matrix is used. To measure the electromechanical response, dog bone samples with a single planar interconnect are fabricated (Figure 3a, inset). First, the sheet resistance of the planar interconnects ϕ = 10, 15 and 20% LM samples was measured and all samples exhibit less than 0.1 Ω/sq (Figure 3a). The electromechanical response of the ϕ= 20% LM sample during bending (50% compressive strain) and unaxial tension (10% strain) was also measured. During the test, the relative electrical resistance maintained a constant level of 1 during both bending (Figure 3b) and tension (Figure 3c).

The LM-STAIR *vias* with ϕ = 10, 15 and 20% LM are measured in the same manner as the planar interconnect (Figure 3d). The sheet resistance of the LM-STAIR *via* is less than 0.3 Ω/sq which is slightly higher compared to the planar interconnects. This is attributed to the longer path length and the lower volume fraction of the LM-STAIR *via* region, as shown in the inset of Figure 3d and S8. Compressive and tensile strain tests are performed with LM-STAIR *via* samples (Figures 3e and f). During the compressive strain test, the bending radius is measured as shown in the inset of Figure 3e. The minimum bending radius is 3.17 mm, and its relative electrical resistance remains constant throughout the test. The

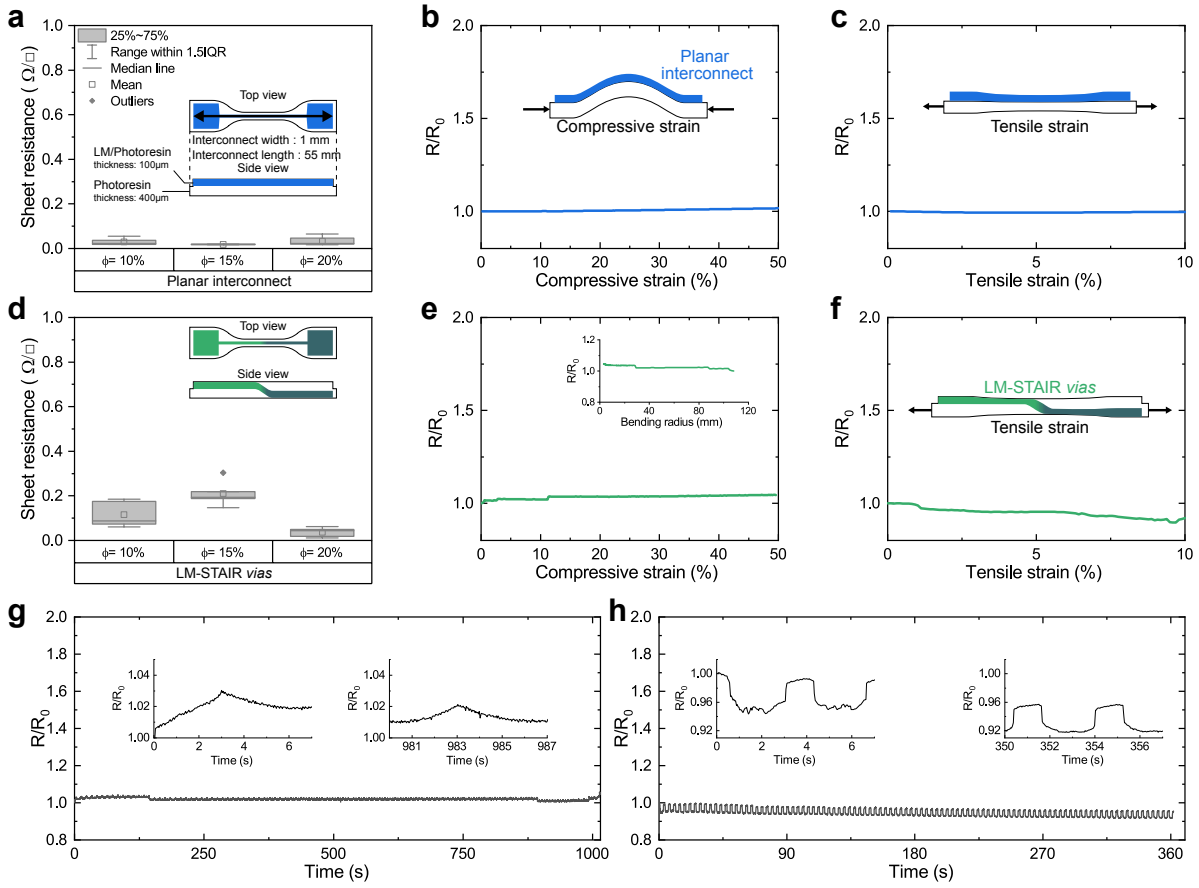

Fig. 3 | Electromechanical characterization of LM-STAIR *vias* and interconnects. **a)** Sheet resistance of the planar interconnect flexible circuit based on the three different LM volume percentages. ($n = 5$ measurements from distinct samples). **b)** Relative electrical resistance of the planar interconnect flexible circuit according to the compressive strain. **c)** Relative electrical resistance of the planar interconnect flexible circuit depending on the tensile strain. **d)** Sheet resistance of LM-STAIR *vias* based on the three different percentages of LM volume. ($n = 5$ measurements from distinct samples). Definition of box plot is same with the **a)** legend. **e)** Relative electrical resistance of the LM-STAIR *via* flexible circuit depending on compressive strain. The inset shows the resistance behavior, depending on the measured bending radius of the specimen. **f)** Relative electrical resistance of the LM-STAIR *vias* flexible circuit depending on the tensile strain. **g)** Durability test of the LM-STAIR *vias* flexible circuit for 100 cycles of compressive strain 50 %. The inset shows the initial and final 7 seconds of the cycle. **h)** Durability test of the flexible LM-STAIR *via* circuit for 100 cycles of 50 % tensile strain. Inset shows initial and final 7 seconds of cycle.

tensile test up to 10% strain also showed a consistent electromechanical response. These results show that the developed LM-STAIR *via* is robust and can withstand different modes of deformation, including folding and stretching. We further examine the electromechanical

durability of the LM-STAIR *vias* with 100 cyclic strain tests that include 50% compressive strain and 10% tensile strain. From both types of strain test, LM-STAIR *via* exhibit a consistent electromechanical response (Figure 3g and h).

After electromechanical characterization, the dielectric constant of the cured photoresin/ diluent without LMMDs is measured. The dielectric constant is a critical factor for signal integrity and impedance matching to make a high-performance electric circuit.[50] The measured dielectric constant is in the range of 3.5 to 4.3 (frequency range of 0.1 to 100 kHz, Figure S15). Considering that the dielectric constant of polyimide that is widely used in flexible commercial electronics is between 3.1 and 3.6, the current polymer matrix is suitable for a substrate material for high performance electrical circuit.[51] Further, environmental stability of the electrical resistance of a LM-STAIR *via* is examined without any additional encapsulation under two different conditions: i) 80 °C elevated temperature and ii) 45 °C underwater (tapwater) (Figure S16). Over 7 days in 80 °C, a slight decrease is observed in normalized resistance (R/R_0=0.87 ± 0.12) while in the elevated temperature the resistance increases slightly the first day then stabilizes (R/R_0=1.31 ± 0.27). This agrees with recent work that has shown the stability of LM-based soft composites in adverse underwater environments,[52] and could likely be further improved with encapsulation if needed. The electromechanical tests results show that the LM-STAIR technique can form and maintain robust electrical interconnections for reliable and flexible circuits.

Multilayer circuit fabrication with 3D interconnects

The LM-STAIR technique successfully electrically connects across circuit layers. Through the LM-STAIR approach, we can also independently control the circuit layout within multiple layers and control connectivity across these layers. To achieve this, we modified the curing direction and sequence to specifically discretize a single layer of LMMDs into multiple layers. This allows planar interconnects to be created that can cross each other in difference layers/planes without being electrically connected except at specified locations where the

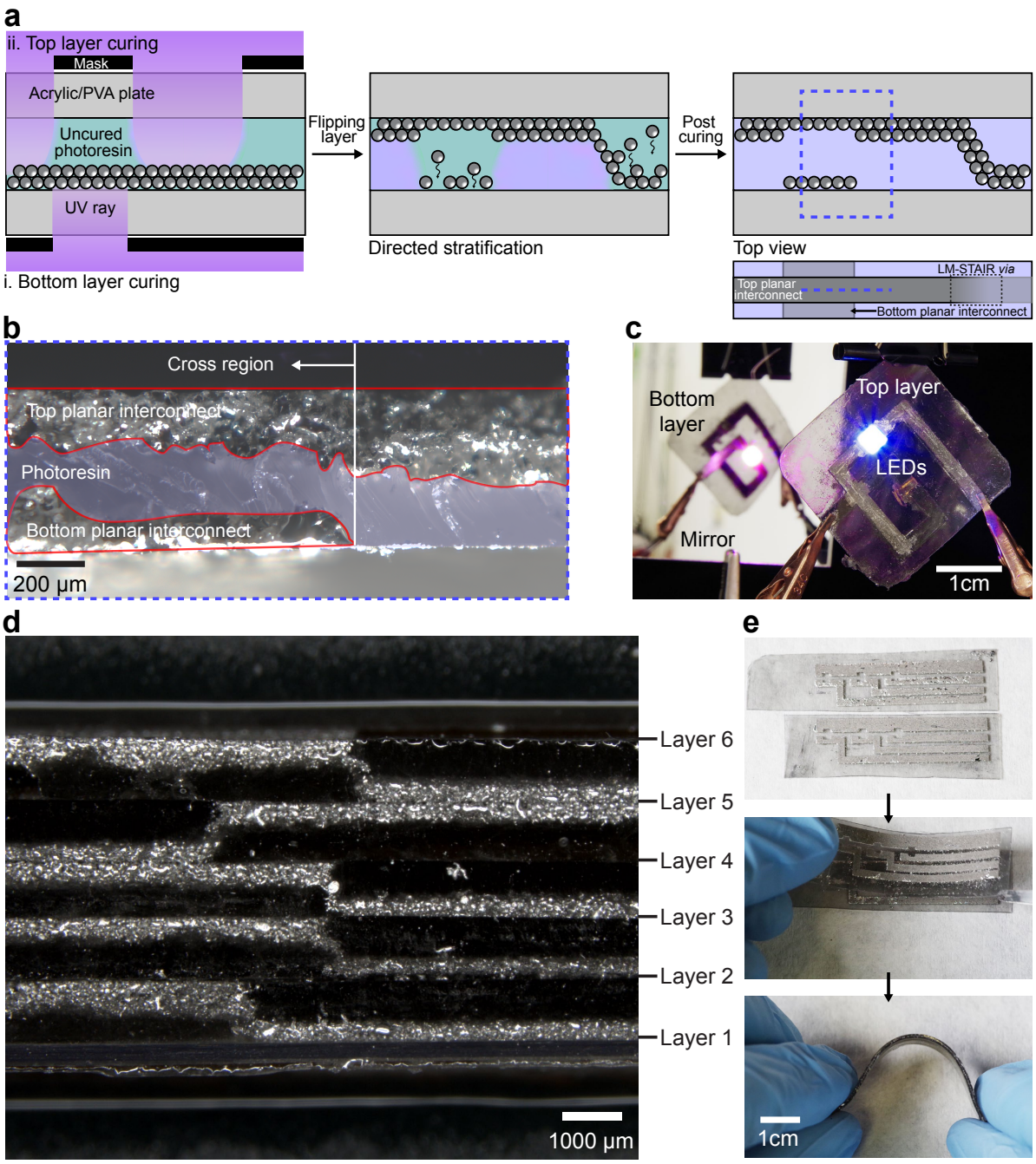

Fig. 4 | Multilayer circuit fabrication with crossing interconnects and adhesion characteristics. **a**, Diagram of cross pattern and LM-STAIR *via* fabrication. **b**, Cross sectional optical microscopic image of the cross pattern. The left half of the image is the cross pattern region. The red dotted area represents the LMMD layers, and the blue shaded area represents photoresin. **c**, Fabricated LED circuit using crossing pattern. **d**, Cross sectional optical microscopy of six soft circuit layers with five *vias* in a single device. **e**, Manual bending test of a pair of adhered LM-STAIR circuits.

LM-STAIR method places soft *vias*. (Figure 4a)

First, we created a single crossing planar interconnect by partially UV curing through the LMMD layer (i.e. UV exposes through the bottom side) (Figure 4a, i. Bottom layer curing). As LMMDs act as UV blockers, the curing of the photoresin is limited to a shallow depth. As a result, this only partially cures the layer of LMMDs. The LMMDs at a greater depth remain in uncured photoresin, which act as the source of LMMDs for the second crossing planar interconnect. The UV exposure time can be used to control this discretization process. Too much curing time locks nearly all LMMDs into the upper position while too little curing time does not lock nearly any LMMDs into the upper position, while an intermediate curing time is able to stratify a single layer of LMMDs into multiple layers (Figure S17). Next, the top side is exposed to UV with a shadow mask placed in the region where the top and bottom planar interconnects will cross (Figure 4a, ii. Top layer curing). During this step, the crossing region is still partially uncured. Then, the LMMDs in the uncured areas (the crossing region and unexposed regions) of the composite are directionally stratified by flipping the layer upside down, while the cured part in the crossing region remains in position. Finally, the entire composite is cured. A cross-sectional micrograph in Figure 4b shows the separation between the top and bottom planar interconnects as a result of this process. The cross-pattern fabrication method is demonstrated with an LED circuit with a cross pattern (Figure 4c). The top and bottom layers of the circuit are illuminated by blue and red LEDs, respectively. This shows the effective creation of crossing planar interconnects, soft *vias*, and independent control of the circuit layout in multiple layers through the LM-STAIR methodology. This technique extends LM-STAIR and allows for the fabrication of intricate intertwined flexible circuits with high complexity. Furthermore, we developed a sequential LM-STAIR technique to create an arbitrary number of soft circuit layers by combining top and bottom curing (Figure S18). Following the normal curing procedure and stratification, by adding another layer of uncured LMMDs/photoresin followed by sequential top and bottom curing, six soft circuit layers with five *vias* were successfully created within a single device structure (Figure

4d).

In addition to the ability to make three-dimensional interconnects, the fabricated flexible circuit can also be stacked together through intrinsic adhesion. The low-modulus surface of the flexible circuits allows for reversible adhesion characteristics. To demonstrate this, two different LM-STAIR fabricated circuits are stacked together (Figure 4e, Supplementary Video 5). The stacked circuits are flexed with no signs of detachment (Figure S19), indicating sufficient adhesion strength to maintain the bond between each layer. After the bending test, the stacked circuits can then be intentionally separated by initiating a crack at an edge and then peeling apart (Figure S20). This adhesion characteristic can be a promising approach for stacking multiple flexible circuits in the future.

Multilayer, dual function flexible circuit demonstration

The proposed LM-STAIR *vias* can electrically connect two different circuit planes in a facile manner. We demonstrate this by fabricating a flexible magnetic field sensing circuit with embedded and interconnected indication circuit. The fabricated flexible circuit has two different layers; a top layer with 9 white LEDs to indicate the magnitude of the magnetic field and a bottom layer with 9 Hall effect sensors to sense the magnetic field (Figure 5a). Hall effect sensor outputs are individually connected to the top layer LED cathode through LM-STAIR *vias*. Connections between the soft circuit and rigid components are made with a paste formed from LM and Cu particles (Figure S21). Even with the complex connection of the electrical components, the thickness of the flexible circuit remained thin (0.33 mm). A total of 21 LM-STAIR soft *vias* and $\sim$ 52 cm long planar interconnects are made (12 *vias* for the cathodes and 9 for the outputs, Figure 5b). These LM-STAIR *vias* seamlessly integrate two different functions. The circuit's on and off state is depicted in the Figure 5c schematic. If there is no magnetic field, the Hall effect sensor output is half the applied voltage (4 V) (Figure 5d). When a magnet is placed 50 mm from the Hall effect sensor, the output is $\sim$2.1 V. At low output voltage, the connected LED does not turn on due to the

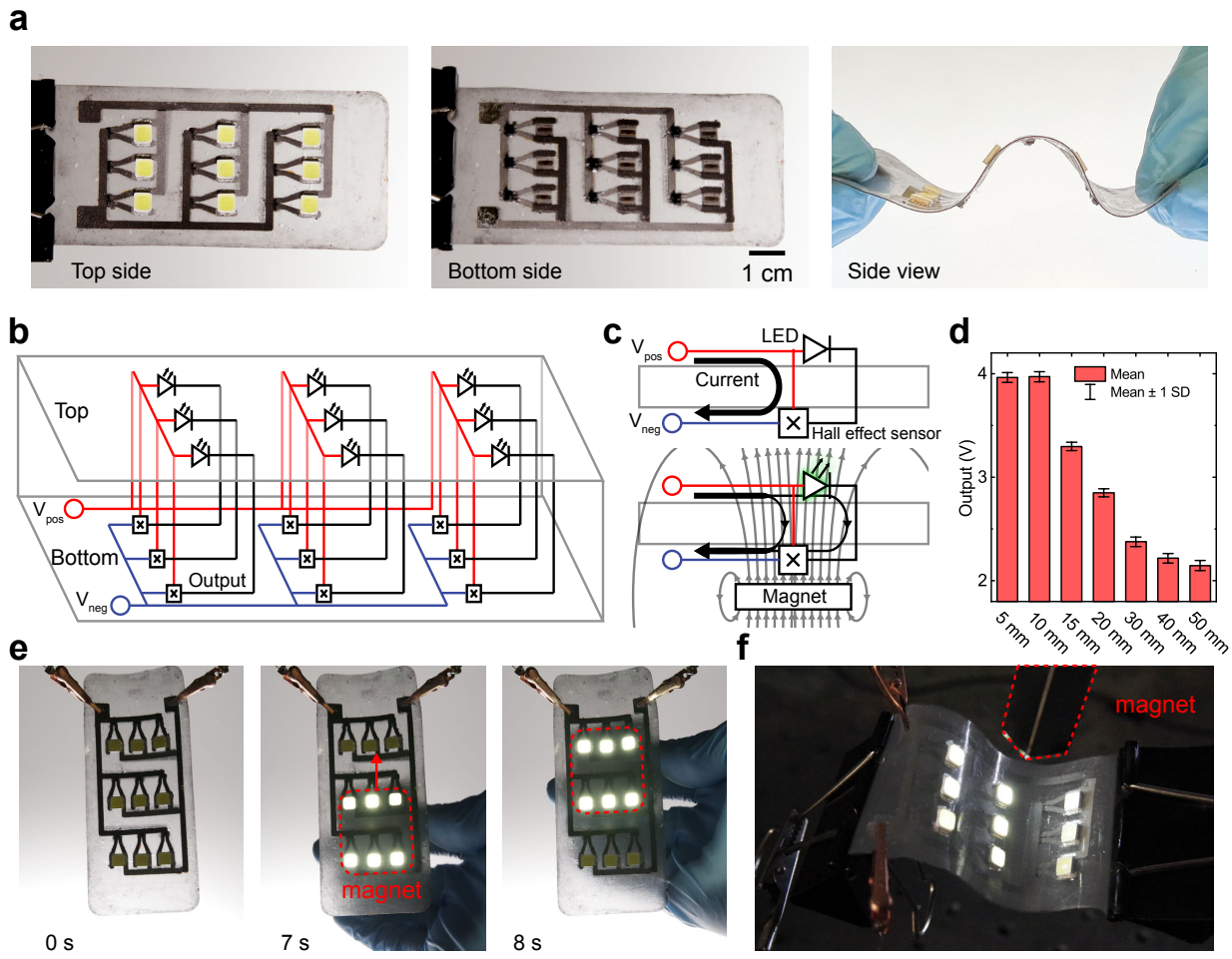

Fig. 5 | Multilayer magnetic sensing and indicating flexible circuit demonstration. **a**, Photography of the magnet sensing and indicating flexible circuit made through the LM-STAIR approach. **b**, Circuit diagram of the magnet sensing and indicating flexible circuit. **c**, Diagram of the Hall effect sensor working mechanism. **d**, Output of the Hall effect sensor depending on the distance of a magnet from the Hall effect sensor. Data are presented as mean ± s.d. for 14000 data points equivalent of 1.4 second. **e**, Photographs of the LEDs illuminated by varying the position of a magnet behind the flexible circuit. **f**, Photograph of the flexible circuit deformed and still functioning as a magnet approaches.

minimum threshold voltage of the LED (3.2 V). After the Hall effect sensor output exceeds the LED threshold voltage, the LED lights up, as shown in the diagram at the bottom of Figure 5c. To demonstrate the fabricated circuit, a rectangular magnet is placed beneath the circuit and moved from the bottom to the top of the circuit (Figure 5e, Supplementary Video 6). It can be observed that only the LEDs near the magnet turn on. Furthermore, the fabricated circuit is bent in an "S" shape to illustrate the robust and soft electrical connec-

tions of LM-STAIR *vias* and planar interconnects (Figure 5f and Supplementary Video 6). The bent circuit performs seamless integration of magnet sensing and indicating functionalities consistently. From these series of demonstrations, the LM-STAIR methodology shows consistent electrical and electromechanical responses, and seamlessly connects two different circuit planes, forming both planar interconnects and soft *vias*.

Conclusions

We have reported a selective photocuring and programmed settling of LM particles fabrication method to rapidly create soft 3D interconnects (soft *vias* and planar interconnects) between different circuit planes. The approach offers a tunable, versatile, and rapid manufacturing process to advance the in-plane and thru-plane integration of soft and flexible electronic devices. Multilayer circuits connected with the technique exhibit high electrical conductivity and mechanical stability, and provide direct electrical and mechanical integration throughout the circuit volume without holes or secondary processes. Because the approach relies on the flow and curing characteristics of the photoresin to position LMMDs throughout the volume, a diverse range of photocurable materials can be used. There is a similar freedom of choice in the LM composition, which can be tuned by a variety of dopants or inclusions for different applications, for example, using iron-doped LM to enable a magneto-responsive composite. As such, future work could leverage a range of different chemistries or inclusion characteristics to broaden the functionality, including responsive systems, biocompatible or biodegradable materials, and multi-material systems.

One challenge that may arise within materials selection is the effect of functional inclusions on the photoresin viscosity. As increased loading of inclusions typically increases viscosity, this could require longer times for the particles to settle. This could be supplemented with techniques to accelerate particle settling, such as using a centrifuge or increasing the temperature to reduce viscosity. However, the programmed stratification technique ef-

fectively concentrates inclusions. Therefore, low inclusion loading before processing become more concentrated during processing, which maintains a working viscosity for rapid processing. Additional topics for future research include down-scaling of feature size through the use of higher resolution patterning methodologies, such as photolithography or e-beam lithography. It may also be possible to automate the fabrication steps to enable mass production of the multilayer soft electronic devices. Thus, the resulting materials and LM-STAIR methodology can serve as the foundation for integrated soft and flexible electronic systems for a variety of functional devices.

Methods

Materials

Photoresin (B9R-2-Black Resin) was obtained from B9Creations. Diluent (Ebecryl 113) was obtained from Allnex. PVA (CAS:9002-89-5, average molecular weight 20000-30000) was obtained from Thermo Scientific. Gallium and Indium (99.99% purity) were obtained from Luceteria Inc.

Fabrication of LM-STAIR *vias*

Detailed fabrication information is described in the Supplementary Note.

Physical characterization

A universal testing machine (Instron 5944) was used to measure the mechanical properties. Electromechanical characterization was performed on a linear stage with a servo motor. The specimen was cut into a dog bone geometry with dimensions specified in Figure 3a. Electrical measurements were performed with a source measurement unit (Keithley 2461). For the demonstration, a DC supply is used to power the LED (MX3AWT-A1-0000-000E50,

CreeLED, Inc.) and Hall effect sensor (A1326LLHLT-T, Allegro MicroSystems) circuitry. The dielectric constant was measured using the BK precision 880 Handheld LCR Meter with four different frequency; 100, 1k, 10k, and 100k. The sample was prepared with a 1 cm circle shape and a thickness of 0.3 mm.

microCT scan

MicroCT was performed on liquid metal composite samples that were manually trimmed from a dog bone-shaped sample and placed on a Kapton with an energy of 60 kV and a resolution of 1.57 µm per voxel (Skyscan 1172 Micro-CT scanner). Manual trimming can result in slight differences in sample dimensions, as seen in Figure 2f, but it does not impact percolation and subsequent sample analysis. The image stack of the reconstructed slides was imported into Avizo software and then threshold segmented to visualize the 3D volume of the liquid metal. The color rendering of the LM phase was performed using open-source software Blender.

Data availability

The data that support the findings of this study are available from the corresponding author upon reasonable request.

Author contribution

D.H.H. and M.D.B. conceived and designed research. D.H.H. conducted research. C.H. and L.L. contributed to measurement and analysis of the microCT scan data. M.D.B. supervised the work. D.H.H. and M.D.B. wrote the paper with contributions from all the authors.

Acknowledgments

D.H.H., and M.D.B. acknowledge support from the Office of Naval Research Young Investigator Program (ONR YIP) (N000142112699) and the National Science Foundation CAREER award (2238754). C.H., and L.L. acknowledge support from Virginia Polytechnic Institute and State University through the COE Faculty Fellowship. C.H. and L.L. also thank Dr. Daniel Baum for the kind assistance in using random-work distance transforms for quantitative microCT analysis.

Competing interests

M.D.B. and D.H.H. are inventors on a patent application (US Patent Application No: 63/535,919) on the fabrication approach. The remaining authors declare no competing interests.

References

[1] Chris A Mack. Fifty years of moore's law. *IEEE Transactions on semiconductor manufacturing*, 24(2):202–207, 2011.

[2] Austin Lancaster and Manish Keswani. Integrated circuit packaging review with an emphasis on 3d packaging. *Integration*, 60:204–212, 2018.

[3] Jeffrey P Gambino, Shawn A Adderly, and John U Knickerbocker. An overview of through-silicon-via technology and manufacturing challenges. *Microelectronic Engineering*, 135:73–106, 2015.

[4] Ryan Hensleigh, Huachen Cui, Zhenpeng Xu, Jeffrey Massman, Desheng Yao, John Berrigan, and Xiaoyu (Rayne) Zheng. Charge-programmed three-dimensional printing for multi-material electronic devices. *Nature Electronics*, 3(4):216–224, 2020.

[5] Steven I. Rich, Robert J. Wood, and Carmel Majidi. Untethered soft robotics. *Nature Electronics*, 1:102–112, 2 2018.

[6] Ryan L Truby, Robert K Katzschmann, Jennifer A Lewis, and Daniela Rus. Soft robotic fingers with embedded ionogel sensors and discrete actuation modes for somatosensitive manipulation. In *2019 2nd IEEE international conference on soft robotics (RoboSoft)*, pages 322–329. IEEE, 2019.

[7] Sarnab Bhattacharya, Mohammad Nikbakht, Alec Alden, Philip Tan, Jieting Wang, Taha A. Alhalimi, Sangjun Kim, Pulin Wang, Hirofumi Tanaka, Animesh Tandon, Edward F. Coyle, Omer T. Inan, and Nanshu Lu. A chest-conformable, wireless electromechanical e-tattoo for measuring multiple cardiac time intervals. *Advanced Electronic Materials*, page 2201284, 2023.

[8] Dae-Hyeong Kim, Nanshu Lu, Rui Ma, Yun-Soung Kim, Rak-Hwan Kim, Shuodao Wang, Jian Wu, Sang Min Won, Hu Tao, Ahmad Islam, Ki Jun Yu, Tae-il Kim, Raeed Chowdhury, Ming Ying, Lizhi Xu, Ming Li, Hyun-Joong Chung, Hohyun Keum, Martin McCormick, Ping Liu, Yong-Wei Zhang, Fiorenzo G. Omenetto, Yonggang Huang, Todd Coleman, and John A. Rogers. Epidermal electronics. *science*, 333(6044):838–843, 2011.

[9] Rui Guo, Xuelin Wang, Hao Chang, Wenzhuo Yu, Shuting Liang, Wei Rao, and Jing Liu. Ni-gain amalgams enabled rapid and customizable fabrication of wearable and wireless healthcare electronics. *Advanced Engineering Materials*, 20(10):1800054, 2018.

[10] Desheng Yao, Huachen Cui, Ryan Hensleigh, Parker Smith, Sam Alford, Dominic Bernero, Sydney Bush, Kyle Mann, H Felix Wu, Marvin Chin-Nieh, Garrett Youmans, and Xiaoyu (Rayne) Zheng. Achieving the upper bound of piezoelectric response in tunable, wearable 3d printed nanocomposites. *Advanced Functional Materials*, 29(42):1903866, 2019.

[11] Hao Zhang and John A Rogers. Recent advances in flexible inorganic light emitting diodes: From materials design to integrated optoelectronic platforms. *Advanced Optical Materials*, 7(2):1800936, 2019.

[12] Steve Park, Michael Vosguerichian, and Zhenan Bao. A review of fabrication and applications of carbon nanotube film-based flexible electronics. *Nanoscale*, 5:1727–1752, 2 2013.

[13] Tsuyoshi Sekitani, Hiroyoshi Nakajima, Hiroki Maeda, Takanori Fukushima, Takuzo Aida, Kenji Hata, and Takao Someya. Stretchable active-matrix organic light-emitting diode display using printable elastic conductors. *Nature materials*, 8(6):494–499, 2009.

[14] Daren Slee, Jeremiah Stepan, Wei Wei, and Jan Swart. Introduction to printed circuit board failures. *2009 IEEE Symposium on Product Compliance Engineering, PSES 2009 - Proceedings*, 12 2009.

[15] Tae Wook Kim, Jong Sung Lee, Young Cheon Kim, Young Chang Joo, and Byoung Joon Kim. Bending strain and bending fatigue lifetime of flexible metal electrodes on polymer substrates. *Materials*, 12:2490, 8 2019.

[16] Junghwan Byun, Eunho Oh, Byeongmoon Lee, Sangwoo Kim, Seunghwan Lee, Yongtaek Hong, J Byun, E Oh, B Lee, S Kim, S Lee, and Y Hong. A single droplet-printed double-side universal soft electronic platform for highly integrated stretchable hybrid electronics. *Advanced Functional Materials*, 27:1701912, 9 2017.

[17] Hamed Shamkhalichenar, Collin J. Bueche, and Jin Woo Choi. Printed circuit board (pcb) technology for electrochemical sensors and sensing platforms. *Biosensors*, 10, 10 2020.

[18] Yuanhang Zhang, Maozhong An, Peixia Yang, and Jinqiu Zhang. Recent advances in electroplating of through-hole copper interconnection. *Electrocatalysis*, 12:619–627, 11 2021.

[19] Wei-Ping Dow, Hsiang-Hao Chen, Ming-Yao Yen, Wei-Hsiang Chen, Kao-Hsuang Hsu, Po-Yao Chuang, Hiroshi Ishizuka, Nobuo Sakagawa, and Ryoichi Kimizuka. Through-hole filling by copper electroplating. *Journal of The Electrochemical Society*, 155:D750, 10 2008.

[20] Khashayar Khoshmanesh, Shi-Yang Tang, Jiu Yang Zhu, Samira Schaefer, Arnan Mitchell, Kourosh Kalantar-Zadeh, and Michael D Dickey. Liquid metal enabled microfluidics. *Lab on a Chip*, 17(6):974–993, 2017.

[21] Michael D Bartlett, Navid Kazem, Matthew J Powell-Palm, Xiaonan Huang, Wenhuan Sun, Jonathan A Malen, and Carmel Majidi. High thermal conductivity in soft elastomers with elongated liquid metal inclusions. *Proceedings of the National Academy of Sciences*, 114(9):2143–2148, 2017.

[22] Michael D Dickey, Ryan C Chiechi, Ryan J Larsen, Emily A Weiss, David A Weitz, and George M Whitesides. Eutectic gallium-indium (egain): a liquid metal alloy for the formation of stable structures in microchannels at room temperature. *Advanced functional materials*, 18(7):1097–1104, 2008.

[23] Selvaraj Veerapandian, Woosun Jang, Jae Bok Seol, Hongbo Wang, Minsik Kong, Kaliannan Thiyagarajan, Junghyeok Kwak, Gyeongbae Park, Gilwoon Lee, Wonjeong Suh, Insang You, Mehmet Emin Kılıç, Anupam Giri, Lucia Beccai, Aloysius Soon, and Unyong Jeong. Hydrogen-doped viscoplastic liquid metal microparticles for stretchable printed metal lines. *Nature materials*, 20(4):533–540, 2021.

[24] Yong Zheng, Hai Liu, Li Yan, Haiyue Yang, Lin Dai, and Chuanling Si. Lignin-based encapsulation of liquid metal particles for flexible and high-efficiently recyclable electronics. *Advanced Functional Materials*, 34(7):2310653, 2024.

[25] Michael D Dickey. Stretchable and soft electronics using liquid metals. *Advanced materials*, 29(27):1606425, 2017.

[26] Xuelin Wang and Jing Liu. Recent advancements in liquid metal flexible printed electronics: Properties, technologies, and applications. *Micromachines*, 7(12):206, 2016.

[27] Sen Chen, Ziliang Cui, Hongzhang Wang, Xuelin Wang, and Jing Liu. Liquid metal flexible electronics: Past, present, and future. *Applied Physics Reviews*, 10:21308, 6 2023.

[28] Michael J Ford, Dinesh K Patel, Chengfeng Pan, Sarah Bergbreiter, and Carmel Majidi. Controlled assembly of liquid metal inclusions as a general approach for multifunctional composites. *Advanced Materials*, 32(46):2002929, 2020.

[29] ABM Tahidul Haque, Dong Hae Ho, Dohgyu Hwang, Ravi Tutika, Chanhong Lee, and Michael D Bartlett. Electrically conductive liquid metal composite adhesives for reversible bonding of soft electronics. *Advanced Functional Materials*, page 2304101, 2023.

[30] Wonbeom Lee, Hyunjun Kim, Inho Kang, Hongjun Park, Jiyoung Jung, Haeseung Lee, Hyunchang Park, Ji Su Park, Jong Min Yuk, Seunghwa Ryu, et al. Universal assembly of liquid metal particles in polymers enables elastic printed circuit board. *Science*, 378(6620):637–641, 2022.

[31] Dong Wu, Shuwang Wu, Poom Narongdej, Sidi Duan, Chi Chen, Yichen Yan, Zixiao Liu, Wen Hong, Imri Frenkel, and Ximin He. Fast and facile liquid metal printing via projection lithography for highly stretchable electronic circuits. *Advanced Materials*, page 2307632, 2024.

[32] Sanhu Liu, Zhiwu Xu, Guoqiang Li, Zhengwei Li, Zihan Ye, Zirong Xu, Wenjun Chen, Dongdong Jin, and Xing Ma. Ultrasonic-enabled nondestructive and substrate-independent liquid metal ink sintering. *Advanced Science*, 10(23):2301292, 2023.

[33] Guolin Yun, Tim Cole, Yuxin Zhang, Jiahao Zheng, Shuaishuai Sun, Yiming Ou-Yang, Jian Shu, Hongda Lu, Qingtian Zhang, Yongjing Wang, Duc Pham, Tawfique Hasan,

Shiwu Zhang, and Shi-Yang Tang. Electro-mechano responsive elastomers with self-tunable conductivity and stiffness. *Science Advances*, 9(4):eadf1141, 2023.

[34] Min Gu Kim, Hommood Alrowais, Spyridon Pavlidis, and Oliver Brand. Size-scalable and high-density liquid-metal-based soft electronic passive components and circuits using soft lithography. *Advanced Functional Materials*, 27:1604466, 1 2017.

[35] Ping Ren and Jingyan Dong. Direct fabrication of via interconnects by electrohydrodynamic printing for multi-layer 3d flexible and stretchable electronics. *Advanced Materials Technologies*, 6(9):2100280, 2021.

[36] Daniel Green Marques, Pedro Alhais Lopes, Anibal T de Almeida, Carmel Majidi, and Mahmoud Tavakoli. Reliable interfaces for egain multi-layer stretchable circuits and microelectronics. *Lab on a Chip*, 19(5):897–906, 2019.

[37] Shanliangzi Liu, Dylan S Shah, and Rebecca Kramer-Bottiglio. Highly stretchable multilayer electronic circuits using biphasic gallium-indium. *Nature Materials*, 20(6):851–858, 2021.

[38] Arthur Hirsch, Hadrien O Michaud, Aaron P Gerratt, Séverine de Mulatier, Stéphanie P Lacour, A Hirsch, H O Michaud, A P Gerratt, S de Mulatier, and S P Lacour. Intrinsically stretchable biphasic (solid–liquid) thin metal films. *Advanced Materials*, 28:4507–4512, 6 2016.

[39] Jangyeol Yoon, Soo Yeong Hong, Yein Lim, Seung-Jung Lee, Goangseup Zi, Jeong Sook Ha, J Yoon, S Y Hong, J S Ha, Y Lim, S j Lee, and G Zi. Design and fabrication of novel stretchable device arrays on a deformable polymer substrate with embedded liquid-metal interconnections. *Advanced Materials*, 26:6580–6586, 10 2014.

[40] Sami Franssila. *Introduction to microfabrication.* John Wiley & Sons, 2010.

[41] Dinesh K Patel, Amir Hosein Sakhaei, Michael Layani, Biao Zhang, Qi Ge, and Shlomo Magdassi. Highly stretchable and uv curable elastomers for digital light processing based 3d printing. *Advanced Materials*, 29(15):1606000, 2017.

[42] Dianpeng Qi, Kuiyuan Zhang, Gongwei Tian, Bo Jiang, and Yudong Huang. Stretchable electronics based on pdms substrates. *Advanced Materials*, 33(6):2003155, 2021.

[43] Byron Llerena Zambrano, Aline F Renz, Tobias Ruff, Samuel Lienemann, Klas Tybrandt, János Vörös, and Jaehong Lee. Soft electronics based on stretchable and conductive nanocomposites for biomedical applications. *Advanced healthcare materials*, 10(3):2001397, 2021.

[44] Michael D Bartlett, Andrew Fassler, Navid Kazem, Eric J Markvicka, Pratiti Mandal, and Carmel Majidi. Stretchable, high-k dielectric elastomers through liquid-metal inclusions. *Advanced Materials*, 28(19):3726–3731, 2016.

[45] Robert W Style, Rostislav Boltyanskiy, Benjamin Allen, Katharine E Jensen, Henry P Foote, John S Wettlaufer, and Eric R Dufresne. Stiffening solids with liquid inclusions. *Nature Physics*, 11(1):82–87, 2015.

[46] Eric J Markvicka, Michael D Bartlett, Xiaonan Huang, and Carmel Majidi. An autonomously electrically self-healing liquid metal–elastomer composite for robust soft-matter robotics and electronics. *Nature materials*, 17(7):618–624, 2018.

[47] Michael J Ford, Cedric P Ambulo, Teresa A Kent, Eric J Markvicka, Chengfeng Pan, Jonathan Malen, Taylor H Ware, and Carmel Majidi. A multifunctional shape-morphing elastomer with liquid metal inclusions. *Proceedings of the National Academy of Sciences*, 116(43):21438–21444, 2019.

[48] Daniel Baum, James C Weaver, Igor Zlotnikov, David Knötel, Lara Tomholt, and Mason N Dean. High-throughput segmentation of tiled biological structures using random-walk distance transforms. *Integrative and comparative biology*, 59(6):1700–1712, 2019.

[49] Nian-Sheng Cheng. Simplified settling velocity formula for sediment particle. *Journal of hydraulic engineering*, 123(2):149–152, 1997.

[50] Eric Bogatin. Essential principles of signal integrity. *IEEE Microwave Magazine*, 12(5):34–41, 2011.

[51] Yu Liu, Xiao-Yu Zhao, Ya-Guang Sun, Wen-Ze Li, Xiao-Sa Zhang, and Jian Luan. Synthesis and applications of low dielectric polyimide. *Resources Chemicals and Materials*, 2(1):49–62, 2023.

[52] Edward J Barron III, Ella T Williams, Brittan T Wilcox, Dong Hae Ho, and Michael D Bartlett. Liquid metal-elastomer composites for water-resilient soft electronics. *Journal of Polymer Science*, 2023.

[53] Taylor V Neumann, Emily G Facchine, Brian Leonardo, Saad Khan, and Michael D Dickey. Direct write printing of a self-encapsulating liquid metal–silicone composite. *Soft Matter*, 16(28):6608–6618, 2020.

Supplementary Information

Soft electronic vias and interconnects through rapid three-dimensional assembly of liquid metal microdroplets

Dong Hae Ho[1,2,3], Chenhao Hu[4,5], Ling Li[4,5], and Michael D. Bartlett[1,2*]

[1]Mechanical Engineering, Soft Materials and Structures Lab, Virginia Tech, Blacksburg, VA 24061, USA.

[2]Macromolecules Innovation Institute, Virginia Tech, Blacksburg, VA 24061, USA.

[3]Present address: Department of Energy Science and Engineering, Daegu Gyeongbuk Institute of Science and Technology (DGIST), Daegu, 42988, Republic of Korea

[4]Mechanical Engineering, Virginia Tech, Blacksburg, VA 24061, USA.

[5]Present address: Department of Materials Science and Engineering, University of Pennsylvania, PA 19104, USA.

*Corresponding author email: mbartlett@vt.edu

Supplementary Notes

Fabrication of LM-STAIR *vias*

Photoresin composite preparation

The material was made of two main parts, the polymer matrix and liquid metal (LM). The polymer matrix consists of two parts, diluent (Ebecryl 113) and photoresin (Black R2, B9 creations). LM was composed of 75 wt% gallium and 25 wt% indium. To control the stretchability and flexibility of the polymer matrix, the wt% of the diluent and photoresin was adjusted. LM added as a volume percentage (ϕ) of the total volume of the emulsion. First, the diluent and LM were poured into the plastic cup according to the final total volume, wt% and ϕ of the composite and mixed with a tongue depressor to break LM into droplets. Second, using a planetary shear mixer(Flacktek Inc.), the LM was dispersed into microsized droplets in the photoresin at 500 RPM for 20 seconds and 2000 RPM for 2 minutes. Shear mixing was performed in a vacuum environment (30 mbar) to eliminate bubbles. After the shear mixing process, the LM/diluent was cooled to room temperature and mixed with the photoresin based on the final wt% of the polymer matrix using a wooden tongue depressor. Finally, the LM/photoresin/diluent was placed on a vibration plate for 5 minutes to avoid micro bubbles inside. For unfilled materials, the same wt% of photoresin/diluent without LM was prepared by shear mixing under the same conditions.

Substrate preparation

To make the flexible and stretchable thin film, two acrylic plates were used as substrates on either side of the fabricated film. Transparent acrylic plates (3 mm thickness) were cut into a rectangular shape (15 cm $\times$ 7 cm) with a laser cutter (Universal Laser Systems, 75 W CO_2 laser) and cleaned using isopropyl alcohol (IPA). After cleaning, the acrylic plate was

placed on a flat surface and a small amount of PVA water solution (20 wt%) is applied to the top side of the acrylic plate. To spread the PVA solution uniformly, a mayer rod (RD specialties, groove size #12) was used. After coating the PVA on the acrylic plate, it was placed in a convection oven at 80 °C for 5 minutes. The same process was repeated on the second plate.

Stencil mask preparation

A stencil mask (Ikonics Imaging, blazer Orange film, 0.1 mm thickness) was cut using a laser cutter. The stencil mask film was composed of 4 layers, adhesives/substrate/adhesives/protective film. The protective film of the stencil mask film was not removed until the curing preparation procedure. The laser cutting machine (Universal Laser Systems, 75 W CO_2 laser) was set to 8-10% laser power with 15% speed using a high Power Density Focusing Optics (HPDFO) lens. This enabled the feature size to be smaller than 200 µm. After the stencil mask was prepared, it was attached to the top of the acrylic plate (PVA-coated side) using a rubber roller.

Curing preparation procedure

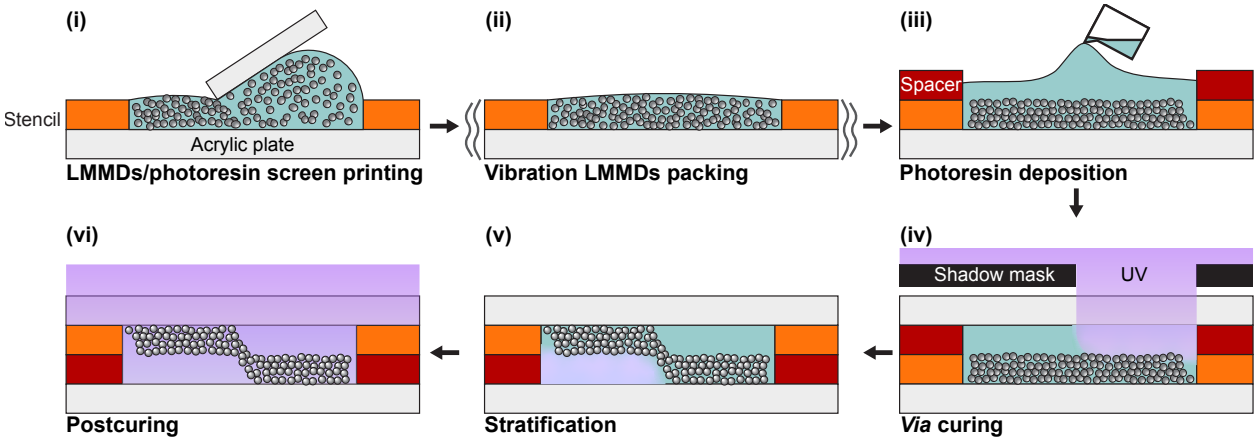

Fig. Note 1 | Fabrication process for LM-STAIR. A schematic process flow diagram for the creation of LM-STAIR *vias* and planar interconnects.

The LM/photoresin was poured on top of an acrylic plate with a stencil mask. LM/photoresin was uniformly spread out using a spatula (Fig. Note 1 (i)). After spreading, a vibrational plate was used to pack the LM microparticles (Fig. Note 1 (ii)). After the LM microparticle packing procedure, excess material was scraped off using a glass slide in one continuous motion. Next, the protective film of the stencil was removed to expose the adhesive and the spacer film (PET, 400 µm) was placed on top. The thickness of the spacer is the primary factor that controls the *via* length. When the T_{spacer} is much greater than the thickness of the LMMD layer ($T_{LMlayer} \ll T_{spacer}$), LMMDs cannot form a continuous connection along the slope due to the greater length of the path (Fig. Note 2a). From 40 to 400 µm, LM-STAIR is formed successfully. However, beyond this thickness range ($T_{spacer} > 500$ µm), LM-STAIR could not be formed due to a depletion of LMMDs along the slope (Fig. Note 2b). This could be addressed in future work if greater thicknesses are required through optimization of $T_{LMlayer}$ through control of LMMD volume loading. The photoresin/diluent was then poured on top of the surface (Fig. Note 1 (iii)). The surface of the meniscus should be higher than the top of the spacer plate to avoid bubbles. Then, an acrylic top plate was placed on top of the spacer (PVA coated side should contact the LM/photoresin) and binder clips were used to clamp the assembly.

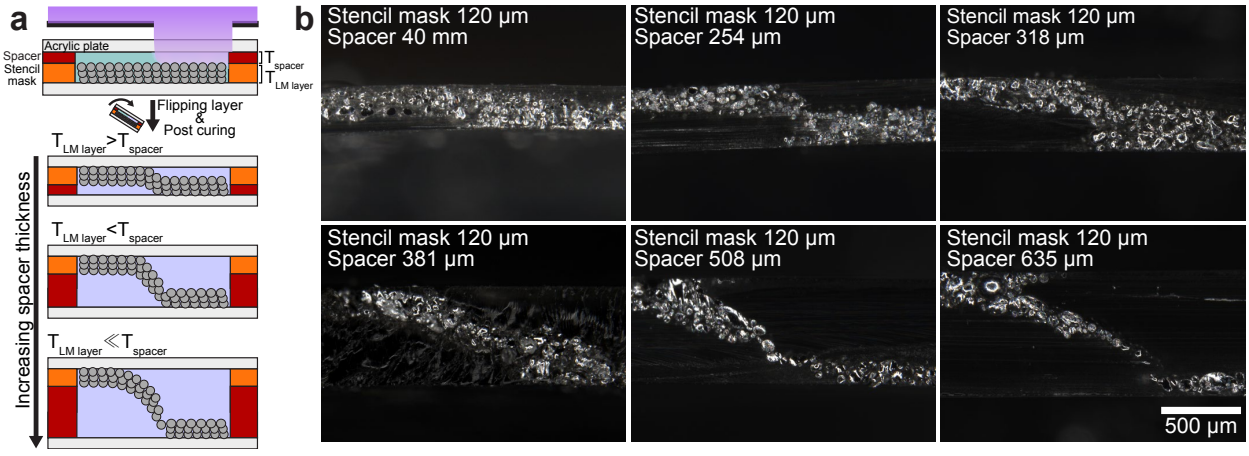

Fig. Note 2 | Photoresin thickness dependant LM-STAIR behavior. a, Schematic of the thickness dependant stratification behavior. **b**, Cross section view of six different photoresin thickness.

Curing Procedure

To cure the LM/photoresin, a UV lamp (380-420 nm, 1000 mW) was located 15 cm above the top surface of the acrylic plate. The shadow mask was placed on top of the acrylic surface, and the UV lamp was turned on for 10 seconds (Fig. Note 1 (iv)). The entire substrate was then flipped. The directed stratification process took less than one minute (Fig. Note 1 (v)). After directed stratification, the top side of the substrate was exposed to UV for 15 seconds to cure the circuit (Fig. Note 1 (vi)). The entire substrate was then cured for 1 minute after removal of the shadow mask. Finally, the fabricated sample was demolded/extracted by peeling off the acrylic plates.

Electrical activation

After assembly and curing, the LMMDs in the *vias* and planar interconnects need to be percolated into continuous networks to become electrically conductive (this process is commonly termed electrical activation or mechanical sintering). This can occur through several different mechanisms. In order to ensure fully conductive networks, we used an embossing method where an acrylic rectangular stamp with a width of 2 mm and a length of 30 mm was pressed by hand into the trace. It is also possible that the samples can become activated during demolding due to the deformation of the sample during peeling, as was previously shown.[53]

Integration of rigid chips onto soft circuit

Rigid electronic components are integrated onto the soft circuits through a paste consisting of 30 wt% copper microparticles (160-400 Mesh, Thermo Fisher Scientific) and LM.

Supplementary Figures

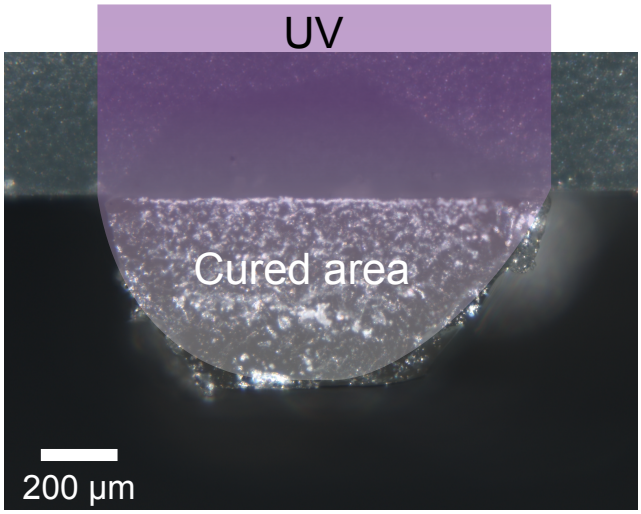

Fig. S1 | Curing behavior of the photoresin by the UV exposure.

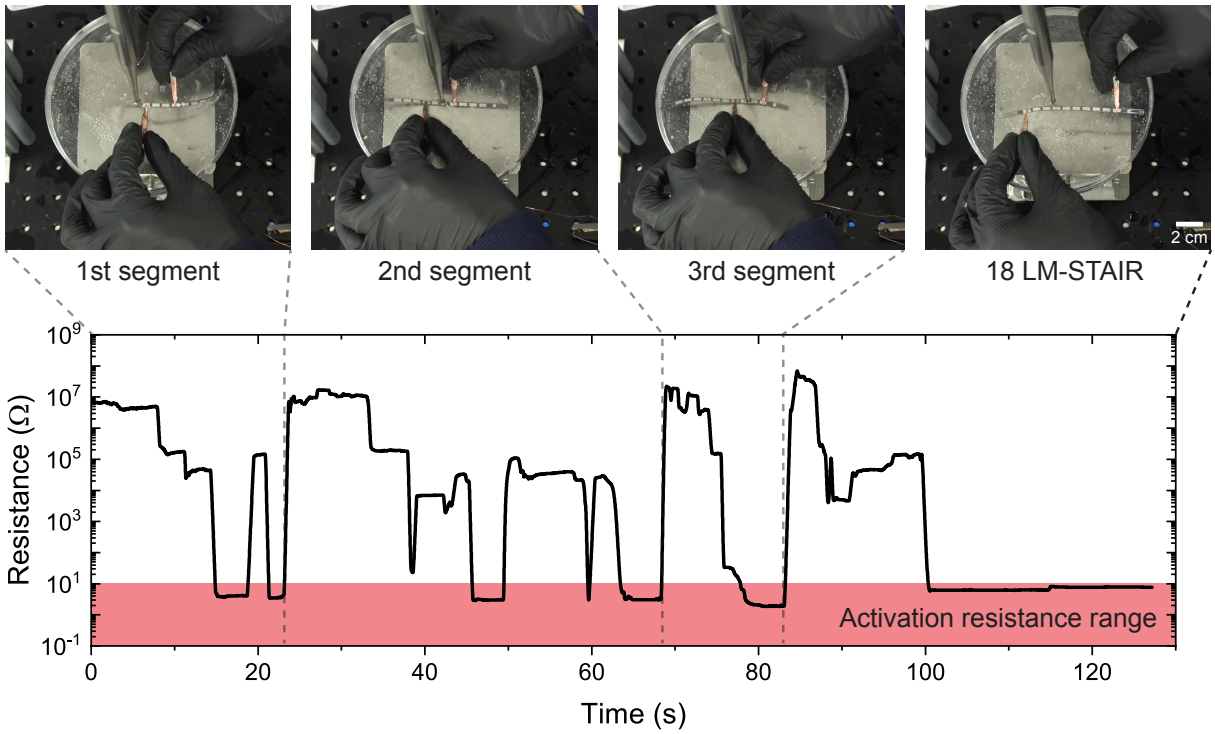

Fig. S2 | Ultrasonic activation of the LMMDs. Ultrasonic activation of LM-STAIR *vias*. 6 LM-STAIR *vias* per segment for three different segments are serially activated for a total of 18 activated LM-STAIR *vias*. Each segment is conductive and the three segments in serial are conductive. Resistance vs. time graph shows the electrical resistance of the sample measured during the whole activation process. The resistance goes up and down as the circuit is connected and disconnected to the different segments, then is connected across all segments at the end to show the serial conductivity.

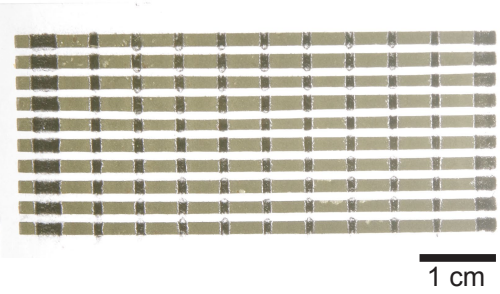

Fig. S3 | Top view of the 200 LM-STAIR *via* sample.

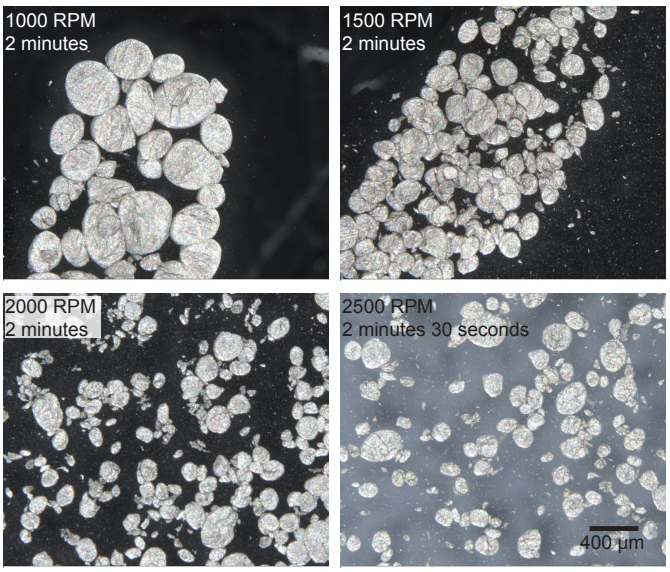

Fig. S4 | Optical microscopic images of different shear mixing conditions. All the images presented in the figure have the same scale bar as shown in the 2000 RPM, 2 minutes 30 seconds.

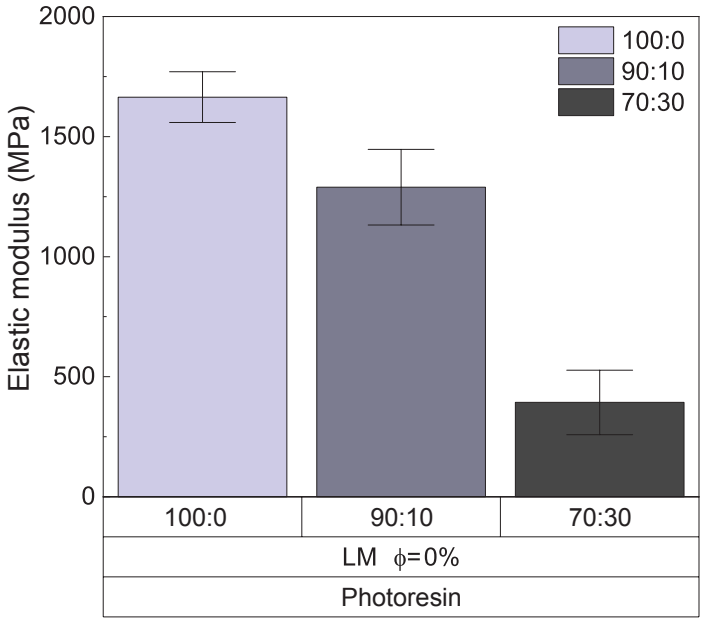

Fig. S5 | Young's modulus based on different weight ratios of photoresin and diluent. The ratio presented in the legend represents the weight ratio of photoresin and diluent (e.g., 30:70 denotes 30 wt% of photoresin and 70 wt% of diluent). Data are presented as the mean ± s.d. ($n = 3$ measurements from distinct samples).

Fig. S6 | Photography of the physical characterization experiments under tensile loading.

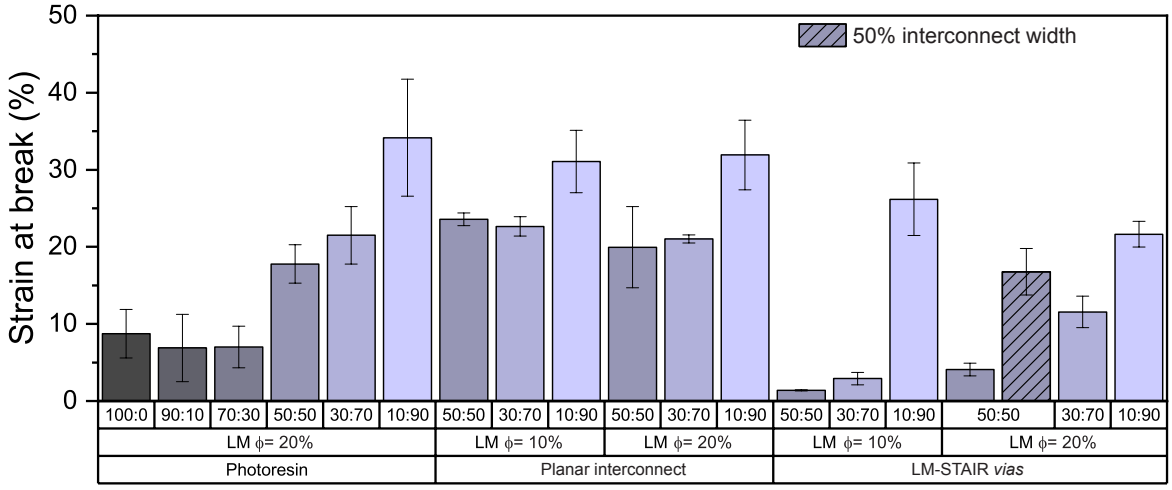

Fig. S7 | Strain at break based on different ratios of photoresin, diluent, and LM volume percentage. The ratio presented in the legend represents the weight ratio of photoresin and diluent (e.g., 30:70 denotes 30 wt% of photoresin and 70 wt% of diluent). LM is added to the photoresin and diluent as the total volume percentage of the composite. Data are presented as the mean ± s.d. ($n = 3$ measurements from distinct samples).

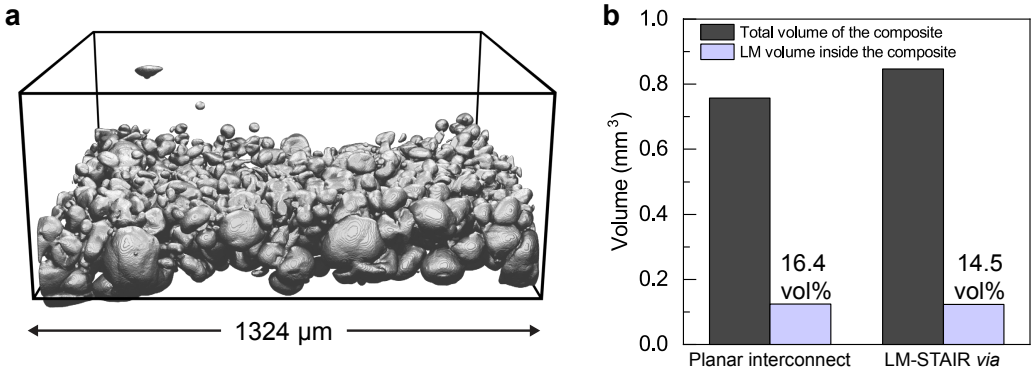

Fig. S8 | Recreated MicroCT images of a planar interconnect and the resulting volume fraction of the LMMDs. a, Three dimensional reconstructed microCT images of a planar interconnect. **b**, Volume fraction of planar interconnect and LM-STAIR *via* based on the reconstructed microCT image.

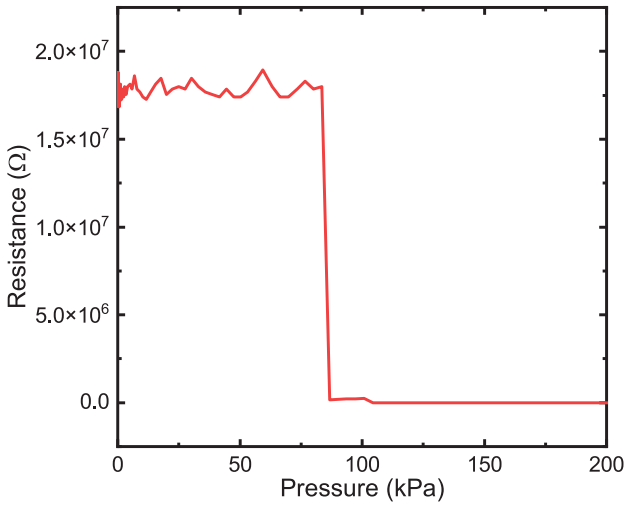

Fig. S9 | Analysis of activation pressure for percolation network formation. The material is 50:50 (50 wt% of photoresin and 50 wt% of diluent) with ϕ= 20%.

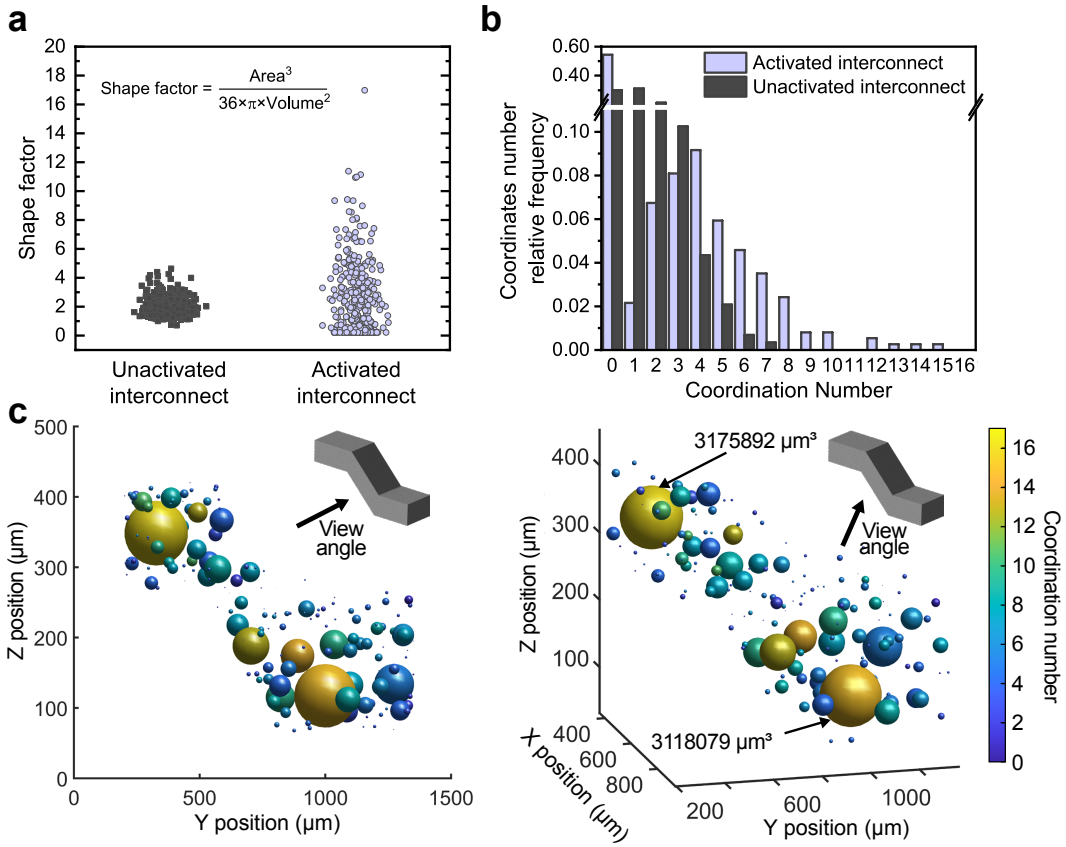

Fig. S10 | LM percolation network analysis based on the reconstructed microCT data using random-walk distance transforms. **a**, Shape factor of unactivated and activated LM percolation network **b**, Coordination number histogram of unactivated and activated LM percolation network **c**, 3D data representation of coordination number and size of each node. Left: perspective perpendicular to the YZ plane, Right: perspective of azimuth angle of 20° and elevation angle of 10°.

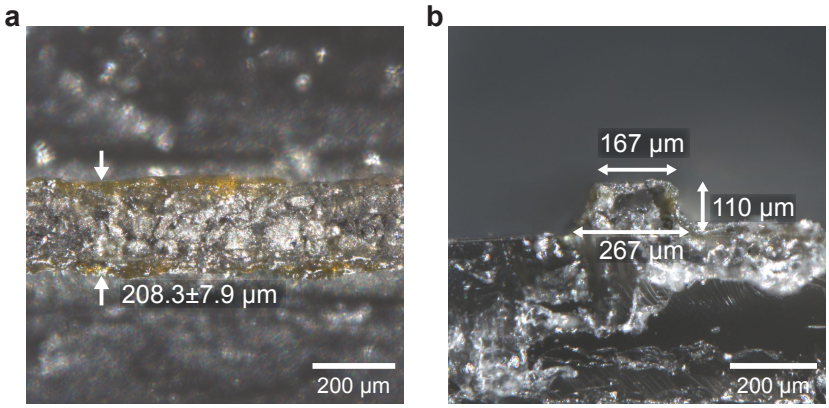

Fig. S11 | Optical micrographs of the minimum feature size for planar interconnects. **a**, Top view. **b**, Side view.

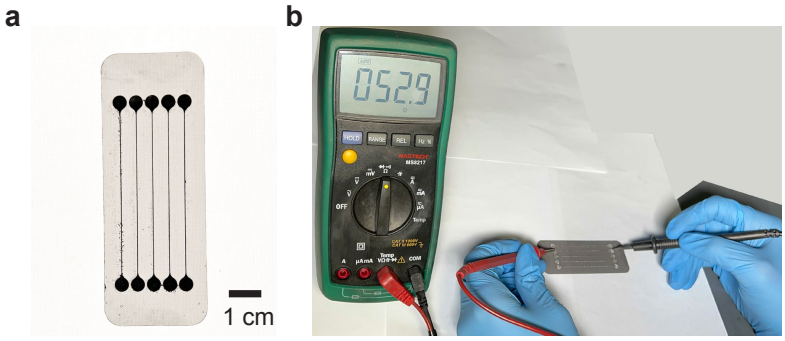

Fig. S12 | Photograph of a minimum feature size specimen and electrical resistance measurement. **a**, Topview of 200 µm feature size sample. **b**, Electrical resistance measurement of the 200 µm feature size planar interconnect showing it is electrically conductive.

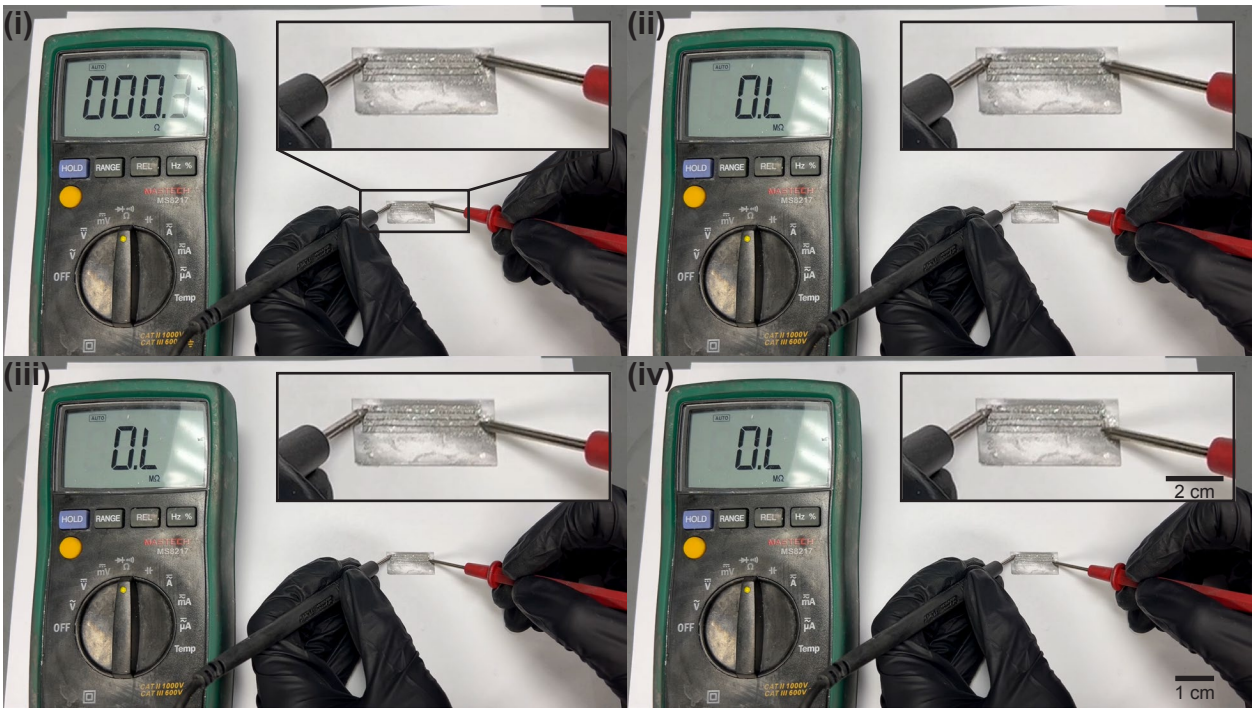

Fig. S13 | Electrical measurement of LMMD trace with 200 μm gap. (i) Single planar interconnect electrical resistance measurement. (ii)-(iv) Adjacent planar interconnects short circuit evaluation.

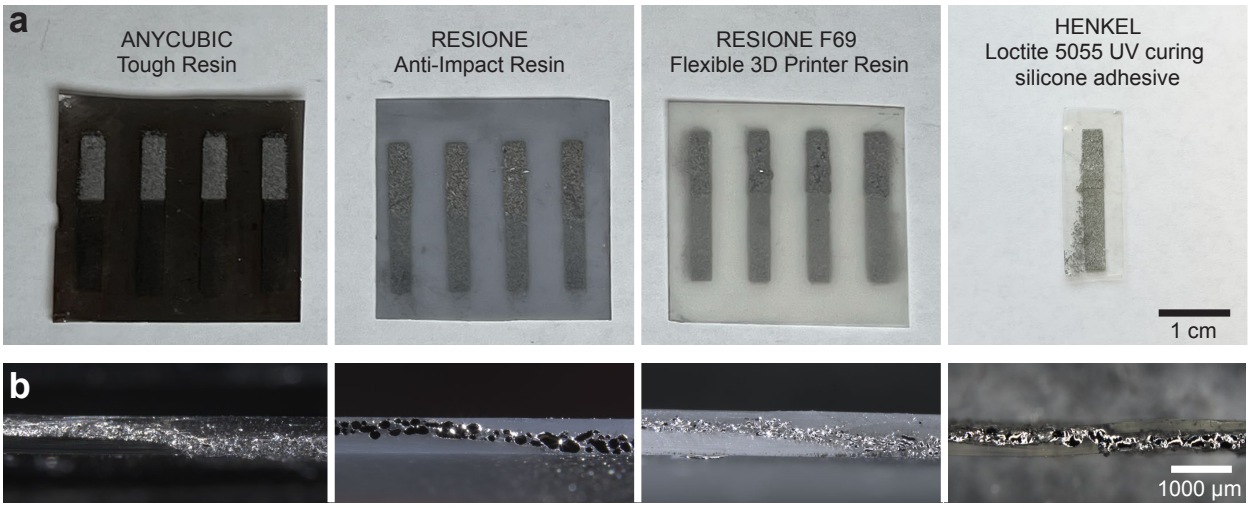

Fig. S14 | LM-STAIR technique performed in various photoresins. **a**, Top view photographs of four different photoresins with *via*. **b**, Cross section view of four different photoresins with *via*.

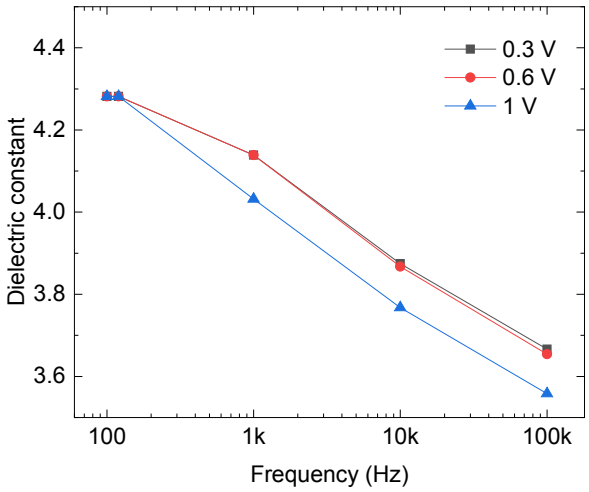

Fig. S15 | Dielectric constant of the photoresin/diluent. Data is presented as a function of frequency for different voltages.

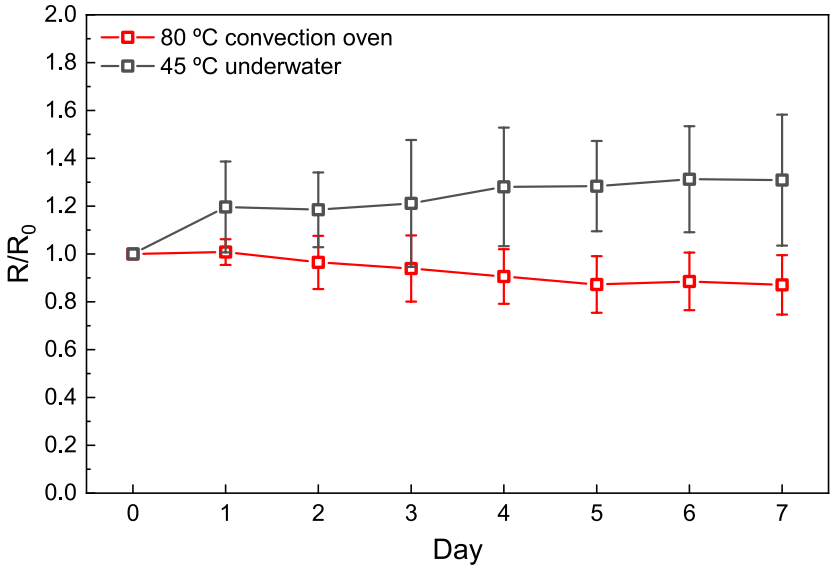

Fig. S16 | LM-STAIR *via* environmental stability test. Samples are aged in two different environments: i) 80 °C elevated temperature and, ii) 45 °C underwater (tapwater). Samples are removed and the resistance is measured (R) and compared to the resistance on day 0 (R_0). Data are presented as the mean ± s.d. ($n = 5$ measurements from distinct samples).

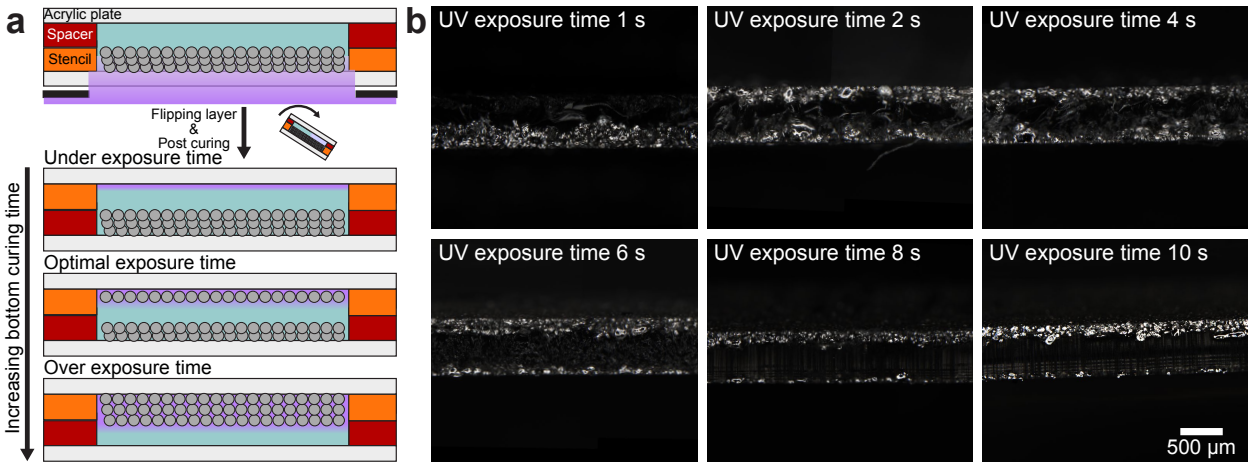

Fig. S17 | Bottom curing time dependant LM-STAIR behavior. **a**, Schematic of the bottom curing time dependant stratification behavior. **b**, Cross section view of six different bottom curing time.

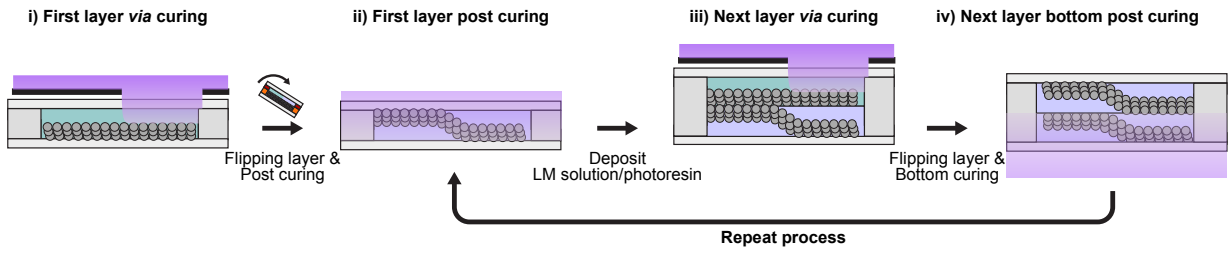

Fig. S18 | Schematic of the multilayer LM-STAIR fabrication technique.

Fig. S19 | Close up photography of bonded circuit under mechanical deformation.

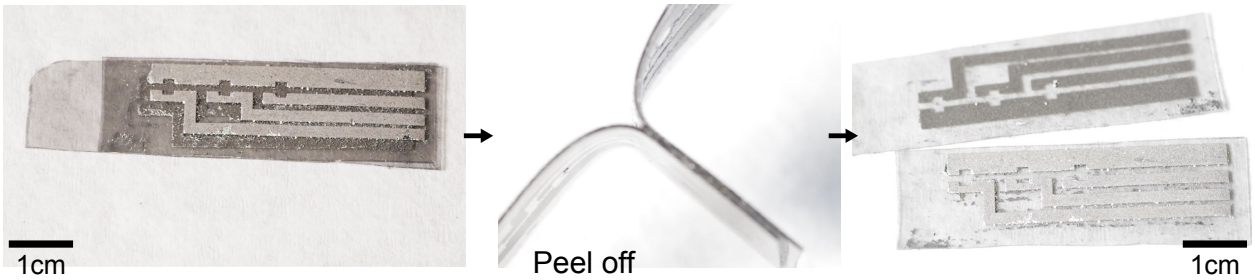

Fig. S20 | Photography of peeling off the LM-STAIR circuits after bending.

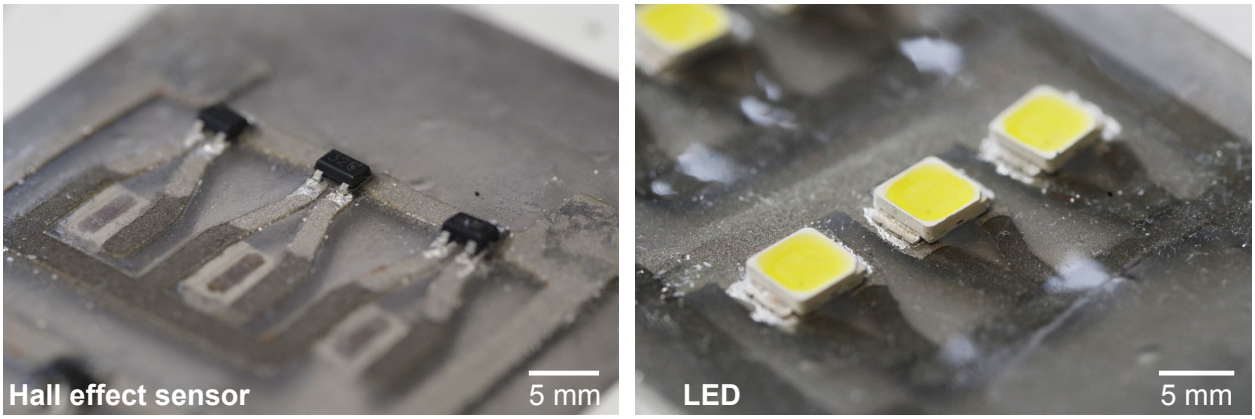

Fig. S21 | Photographs of terminal of Hall effect sensor and LED.

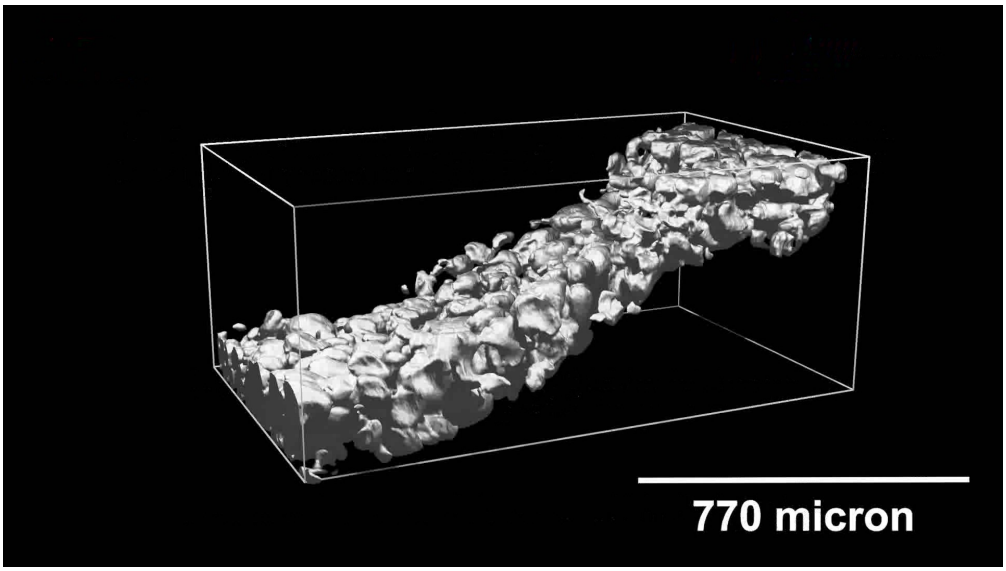

Supplementary Video 1: Reconstructed microCT image of an LM-STAIR *via*. This 360 degree rotation video shows a LM-STAIR *via* that seamlessly connects the top and bottom layers through electrically conductive LMMDs. The 3D model is reconstructed from the microCT scan.

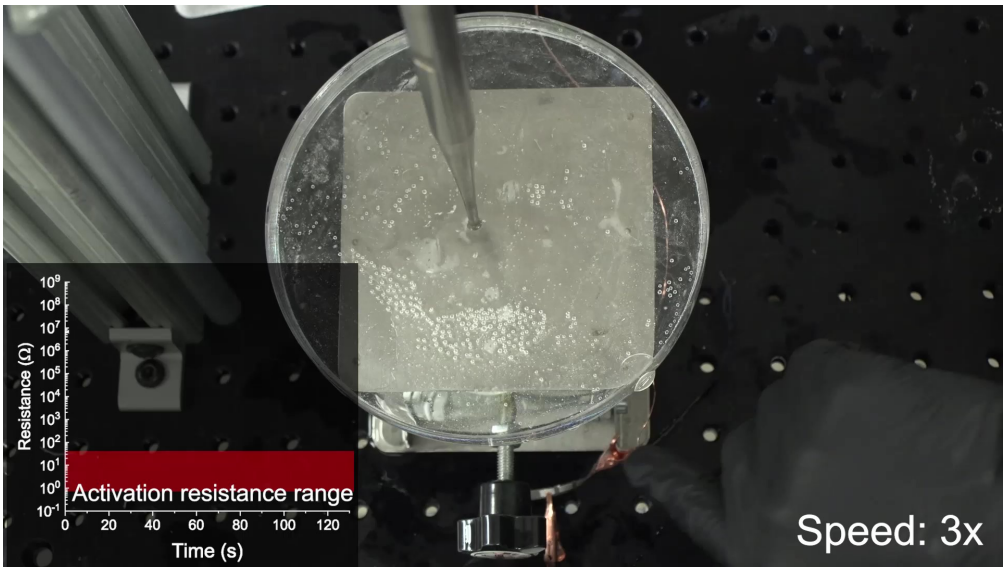

Supplementary Video 2: Realtime ultrasonic activation of 18 LM-STAIR *vias*. This video shows the realtime ultrasonic activation of LM-STAIR *vias*. 6 LM-STAIR *vias* per segment for three different segments are serially activated for a total of 18 activated LM-STAIR *vias*. Each segment is conductive and the three segments in serial are conductive. The electrical resistance of the sample is measured during the whole activation process and is compiled as a resistance vs. time graph. The resistance goes up and down as the circuit is connected and disconnected to the different segments, then is connected across all segments at the end to show the serial conductivity.

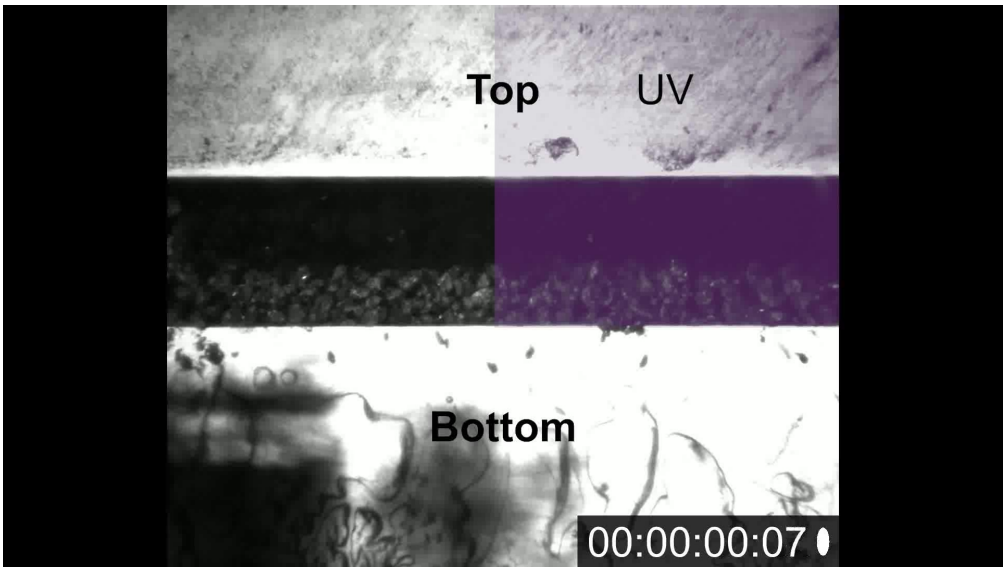

Supplementary Video 3: Realtime fabrication of LM-STAIR *vias*. This video shows the realtime directed stratification of LMMDs inside the photoresin. The right side of the sample is exposed to UV radiation to cure the photoresin. After UV exposure, the layer is flipped upside down and the LMMDs on the uncured side are stratified to the bottom layer. During directed stratification, LMMDs are assembled on top of the undercut region. The LM-STAIR *via* process takes less than a minute to complete.

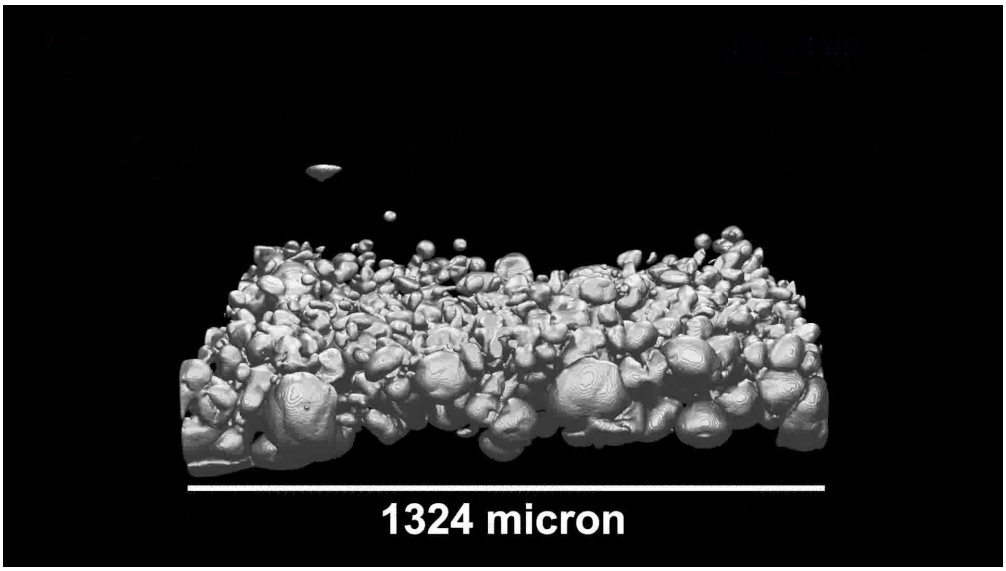

Supplementary Video 4: Reconstructed microCT images of a planar interconnect. This 360 degree rotation video shows the planar interconnect composed of LMMDs. The 3D model is reconstructed from the microCT scan.

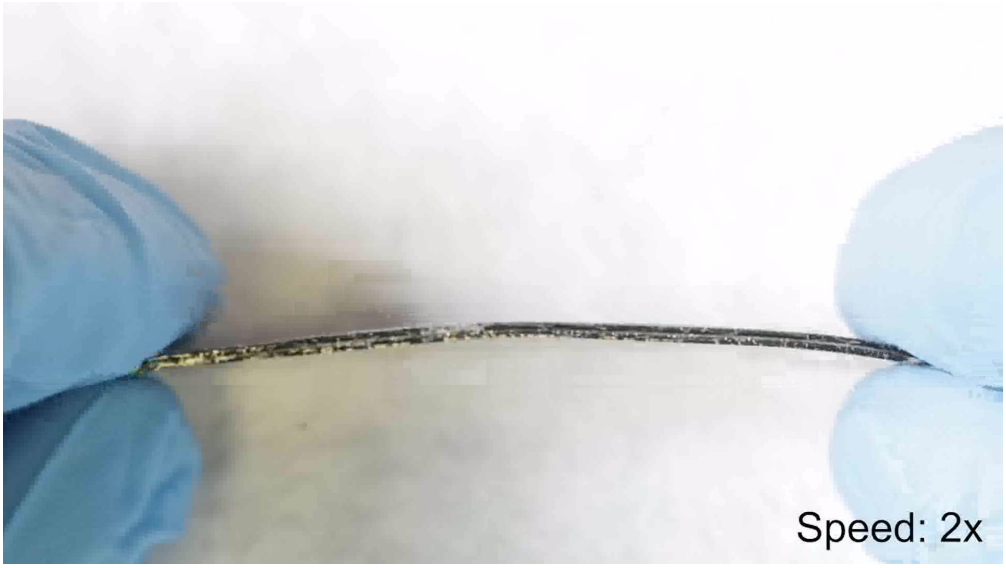

Supplementary Video 5: Circuit adhesion demonstration. This video displays bending of the bonded circuit. The intrinsic adhesion characteristics of the photoresin/diluent composite bond two circuits together during bending deformation. After bending deformation, the two circuit layers are manually separated.

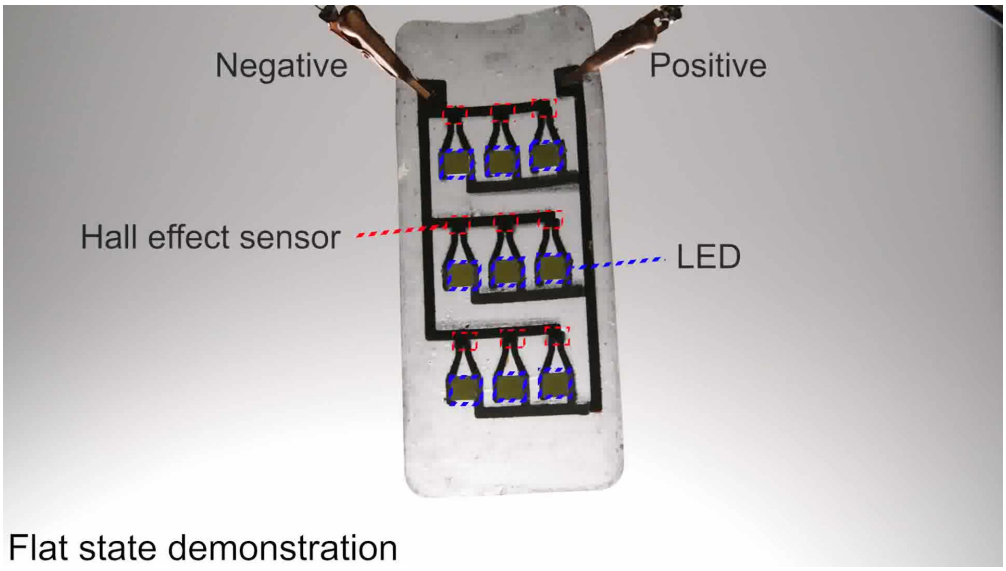

Supplementary Video 6: Multilayer magnetic sensing and indicating flexible circuit demonstration. This video shows a demonstration of fabricated double side electric circuit. A rectangular magnet is placed beneath the circuit and moved from the bottom to the top of the circuit. It can be observed that only the LEDs near the magnet turn on. Then, the fabricated circuit is bent in an "S" shape to illustrate the robust and soft electrical connections of LM-STAIR *vias* and planar interconnects. The bent, multilayer circuit performs seamless integration of magnet sensing and indicating functionalities.